

Active Learning for Finite Element Simulations with Adaptive Non-Stationary Kernel Function

Romain Boutelet and Chih-Li Sung*

Michigan State University

Abstract

Simulating complex physical processes across a domain of input parameters can be very computationally expensive. Multi-fidelity surrogate modeling can resolve this issue by integrating cheaper simulations with the expensive ones in order to obtain better predictions at a reasonable cost. We are specifically interested in computer experiments that involve the use of finite element methods with a real-valued tuning parameter that determines the fidelity of the numerical output. In these cases, integrating this fidelity parameter in the analysis enables us to make inference on fidelity levels that have not been observed yet. Such models have been developed, and we propose a new adaptive non-stationary kernel function which more accurately reflects the behavior of computer simulation outputs. In addition, we aim to create a sequential design based on the integrated mean squared prediction error (IMSPE) to identify the best design points across input parameters and fidelity parameter, while taking into account the computational cost associated with the fidelity parameter. We illustrate this methodology through synthetic examples and applications to finite element analysis. An R package for the proposed methodology is provided in an open repository.

Keywords: Surrogate model; Finite element methods; Sequential design; Multi-fidelity model; Uncertainty quantification; Gaussian process.

*These authors gratefully acknowledge funding from NSF DMS 2338018.

1 Introduction

Computer simulations are pivotal across diverse scientific fields ranging from plant biology to aerospace engineering. High-fidelity simulations, while highly accurate, often require substantial computational resources and time. For instance, a large-eddy simulation of a single injector design in Mak et al. (2018) can take six days of computation, even when parallelized over 200 CPU cores.

To address these computational challenges, multi-fidelity simulations have emerged as a practical solution. These simulations leverage a combination of low-fidelity and high-fidelity models. Low-fidelity simulations are computationally cheaper but less accurate, whereas high-fidelity simulations offer greater accuracy at a higher computational cost. A statistical model, or *emulator*, integrates data from both fidelity levels to generate accurate predictions efficiently. When simulations are costly to run, emulators become indispensable tools, particularly for exploring a wide range of input variables. The foundational work by Kennedy and O’Hagan (2000) has significantly impacted this approach by modeling a sequence of computer simulations from lowest to highest fidelity using a series of stationary Gaussian process (GP) models linked by a linear auto-regressive framework. Subsequent developments inspired by this approach include Qian et al. (2006), Le Gratiet (2013), Le Gratiet and Garnier (2014), Qian and Wu (2008), Perdikaris et al. (2017), Ji et al. (2024a), and Heo and Sung (2025), among others.

Finite element analysis (FEA) exemplifies the need for multi-fidelity approaches (Brenner and Scott, 2007). FEA is widely used to simulate real-world phenomena such as soil erosion and climate change, involving tuning parameters like mesh density that control numerical accuracy and computational cost. Coarser meshes in FEA are less costly but less accurate, whereas finer meshes provide higher accuracy at increased computational expense. Tuo et al. (2014) first incorporated the tuning parameters in the statistical model, introducing a *non-stationary* GP model consistent with numerical analysis results, to emulate the exact solution at its finest mesh. This model has been further developed for conglomerate multi-fidelity emulation (Ji et al., 2024b).

Despite these advancements, important gaps remain in the *design* of multi-fidelity

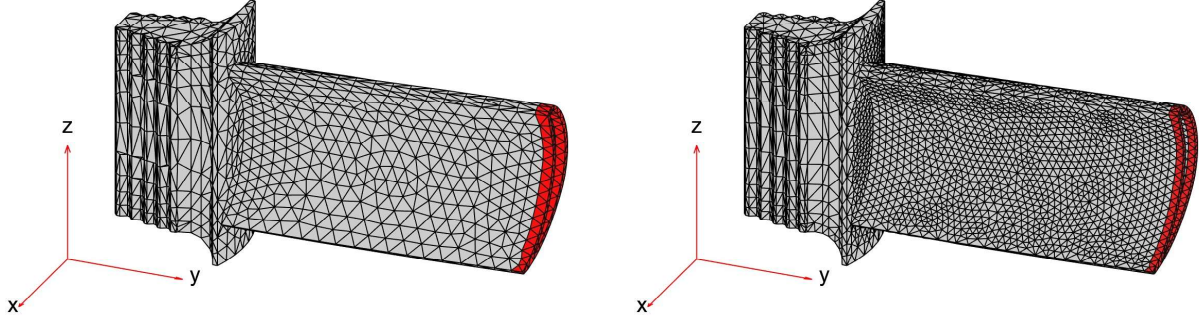


Figure 1: Visualizing the FEA mesh generation for two choices of mesh sizes ($t = 0.01$ on the left and $t = 0.005$ on the right) in the turbine blade application. The red cells indicate the area of interest.

experiments with tuning parameters for cost-efficient emulation. Notable exceptions include the recent work by Shaowu Yuchi et al. (2023), which introduced one-shot, batch designs for multi-fidelity finite element simulations based on the model of Tuo et al. (2014), and the work by Sung et al. (2024), which proposed sequential batch designs based on the auto-regressive model of Kennedy and O’Hagan (2000).

This study addresses these critical gaps through two groundbreaking contributions. First, we propose a novel, *adaptive* non-stationary kernel function, inspired by fractional Brownian motion, to enhance the model by Tuo et al. (2014). This advanced structure accommodates varying degrees of positive correlation in simulation increments across different tuning parameter values, making it particularly advantageous for multi-fidelity finite element simulations. This enhancement not only improves prediction performance but also ensures better consistency with numerical analysis results, positioning Tuo et al. (2014)’s model as a special case within this more comprehensive framework.

Second, we introduce an innovative active learning (AL) framework. In contrast to the batch designs used by Shaowu Yuchi et al. (2023) and Sung et al. (2024), active learning, also known as sequential design, selects new design points one at a time based on optimizing a criterion that evaluates the model’s predictive performance. This iterative, step-by-step method is not only more practical but often proves more effective than static batch designs (Gramacy, 2020). We employ the integrated mean squared prediction error (IMSPE) as the criterion for AL, taking simulation costs into account. Inspired by Binois et al. (2019),

we show that solving this sequential design problem efficiently involves deriving a closed-form expression for IMSPE and its derivatives, enabling fast numerical optimization. In addition, we explore the challenge of selecting an adequate initial design for the active learning approach, already explored by Song and Joseph (2025) in the context of dimension reduction, highlighting the need for a balance between space-filling properties and robust parameter estimation.

The rest of the paper is organized as follows: Section 2 introduces the proposed emulator with an adaptive non-stationary kernel. Section 3 outlines the AL approach, detailing IMSPE with a focus on sequential applications, computational improvements, and initial designs. Sections 4 and 5 present numerical and real data studies, respectively. Finally, the paper concludes in Section 6.

2 Multi-Fidelity Modeling for Finite Element Analysis

We first present the surrogate model used in this paper in Section 2.1, and we introduce our novel kernel function adapted to the FEA simulations in Sections 2.2 and 2.3. We finally give additional details on inference in Sections 2.4.

2.1 Non-Stationary GP Surrogate Model

We study the computer output $y(\mathbf{x}, t)$ at the parameter input $\mathbf{x} \in \mathcal{X} \subset \mathbb{R}^d$, and for mesh size $t \in \mathcal{T}$, where \mathcal{T} denotes the space of possible mesh densities. We only consider the case where t is a non-negative scalar. We adopt the general non-stationary model introduced in Tuo et al. (2014). The approximate solution from the computer simulation $y(\mathbf{x}, t)$ is represented as the sum of the *exact/true solution* to this physical model, denoted by $\varphi(\mathbf{x}) := y(\mathbf{x}, 0)$, and the error function $\delta(\mathbf{x}, t)$ with respect to the mesh density t :

$$y(\mathbf{x}, t) = \varphi(\mathbf{x}) + \delta(\mathbf{x}, t), \quad (\mathbf{x}, t) \in \mathcal{X} \times \mathcal{T}. \quad (1)$$

In this model, the functions $\varphi(\mathbf{x})$ and $\delta(\mathbf{x}, t)$ are assumed to be realizations of Gaussian processes (GPs), a probabilistic framework often used to approximate expensive computer

simulations (Gramacy, 2020). A GP $Y(\mathbf{x})$ is uniquely determined by its mean function $\mu(\mathbf{x})$ and its covariance function $K(\mathbf{x}_1, \mathbf{x}_2)$. More specifically, a GP is said to be stationary if μ is constant, and K can be expressed as a function of the difference between \mathbf{x}_1 and \mathbf{x}_2 , i.e., $K(\mathbf{x}_1, \mathbf{x}_2) = \sigma^2 R(\mathbf{x}_1 - \mathbf{x}_2)$, where σ^2 is the variance and R is the corresponding correlation function. For simplicity, we will here use the Gaussian separable correlation function $R_\phi(\mathbf{h}) = \exp\left(-\sum_i \phi_i^2 h_i^2\right)$, where $\phi^2 = (\phi_i^2)_i$ is the vector of correlation parameters along each dimension.

We assume that the true solution $\varphi(\mathbf{x})$ is a realization of a non-stationary GP denoted by V with the mean function $\mu_V(\mathbf{x}) = \mathbf{f}_V(\mathbf{x})^T \boldsymbol{\beta}_1$, and covariance function

$$K_V(\mathbf{x}_1, \mathbf{x}_2) = \sigma_1^2 R_{\phi_1}(\mathbf{x}_1 - \mathbf{x}_2).$$

Similarly, we assume that the error function $\delta(\mathbf{x}, t)$ is a realization of a non-stationary GP denoted by Z with the mean function $\mu_Z(\mathbf{x}, t) = \mathbf{f}_Z(\mathbf{x}, t)^T \boldsymbol{\beta}_2$, and a separable covariance function in regards to the mesh size and input parameter:

$$K_Z((\mathbf{x}_1, t_1), (\mathbf{x}_2, t_2)) = \sigma_2^2 R_{\phi_2}(\mathbf{x}_1 - \mathbf{x}_2) K_H(t_1, t_2)^l,$$

where $K_H(t_1, t_2)$ defines the dependency structure between different mesh sizes, and l is a predefined parameter that relates to the convergence rate of the solution.

The response variable $y(\mathbf{x}, t)$ is then a realization of a GP $\{Y(\mathbf{x}, t) : (x, t) \in \mathcal{X} \times \mathcal{T}\}$ with the mean $\mu(\mathbf{x}) = \mu_V(\mathbf{x}) + \mu_Z(\mathbf{x}, t) = \mathbf{f}(\mathbf{x}, t)^T \boldsymbol{\beta}$, where $\mathbf{f}(\mathbf{x}, t)^T = (\mathbf{f}_V(\mathbf{x})^T, \mathbf{f}_Z(\mathbf{x}, t)^T)$ and $\boldsymbol{\beta} = (\boldsymbol{\beta}_1^T, \boldsymbol{\beta}_2^T)^T \in \mathbb{R}^p$, and the covariance function

$$K((\mathbf{x}_1, t_1), (\mathbf{x}_2, t_2)) = \sigma_1^2 R_{\phi_1}(\mathbf{x}_1 - \mathbf{x}_2) + \sigma_2^2 R_{\phi_2}(\mathbf{x}_1 - \mathbf{x}_2) K_H(t_1, t_2)^l. \quad (2)$$

As outlined in Tuo et al. (2014), the convergence of FEA methods are well studied and the error function δ can be controlled. In particular, with some assumptions, if we use the L_2 -norm, then $\|\delta\|_{L_2} \leq c t^2 \|\varphi''\|_{L_2}$, where c is a constant independent of t and $\|\varphi''\|_{L_2} = \left(\sum_{i,j} \left\|\frac{\partial^2 \varphi}{\partial x_i \partial x_j}\right\|\right)^{\frac{1}{2}}$ (Brenner and Scott, 2007). This convergence of the error

function can be leveraged through inducing non-stationarity in the surrogate model, by including some assumptions to ensure that as t gets closer to zero, the output of the computer simulation gets closer to the exact solution. We therefore assume that $\mu_Z(\mathbf{x}, t) \rightarrow 0$ as $t \rightarrow 0$, and $K_H(t_1, t_2) \rightarrow 0$ as $\min(t_1, t_2) \rightarrow 0$. In addition, the assumed convergence rate of the solution l can be determined based on this upper bound. For example, for the L_2 -norm, we have that $l = 4$. More details can be found in Tuo et al. (2014). From these constraints, we deduce that Z must have a non-stationary covariance function that reflects the convergence of the error function, which will be induced through the kernel function K_H .

2.2 Novel Adaptive Kernel Function

Given the necessity of providing Z an appropriate non-stationary kernel function, we introduce a novel adaptive mesh size kernel function K_H .

Previous works considered two different forms for the non-stationary covariance function: $K_H(t_1, t_2) = \min(t_1, t_2)$ or $K_H(t_1, t_2) = \sqrt{t_1 t_2} \exp\{-\phi^2(t_1 - t_2)^2\}$ (Tuo et al., 2014), representing respectively uncorrelated increments of the simulation errors, known as a Brownian motion (BM), or a scaled stationary process (SSP). Inspired by the fractional Brownian motion (FBM), we propose to use

$$K_H(t_1, t_2) = \left[\frac{1}{2}(t_1^{2H} + t_2^{2H} - |t_1 - t_2|^{2H}) \right]^{\frac{1}{2H}},$$

an extension of the BM kernel ($H = 0.5$) that generalizes the model to any degree of correlation in the increments. This new kernel is motivated by observations of positively correlated (Figure 3), and negatively or non-correlated (Figure 8) increments of the output, highlighting the need for a more flexible kernel that takes advantage of these features to obtain better extrapolation of the true solution.

To illustrate the effect of the choice of the kernel function K_H , we plot the sample paths from a synthetic example taken from Tuo et al. (2014). Let the exact solution be $\varphi(x) = \exp\{-1.4x\} \cos(3.5\pi x)$. We then use the surrogate model to create 6 sample paths at different mesh sizes and compare those sample paths for different error correlation factors

$H \in \{0, 0.5, 1\}$. The different patterns can be observed in Figure 2. For a fixed point x_0 , we observe that the increments $y(x_0, t + h) - y(x_0, t)$ are perfectly correlated in the case $H = 1$, independent in the case $H = 0.5$, and negatively correlated in the case $H = 0$. This allows the model to incorporate any degree of positive or negative correlation in the increments, making it flexible for various dependency structures.

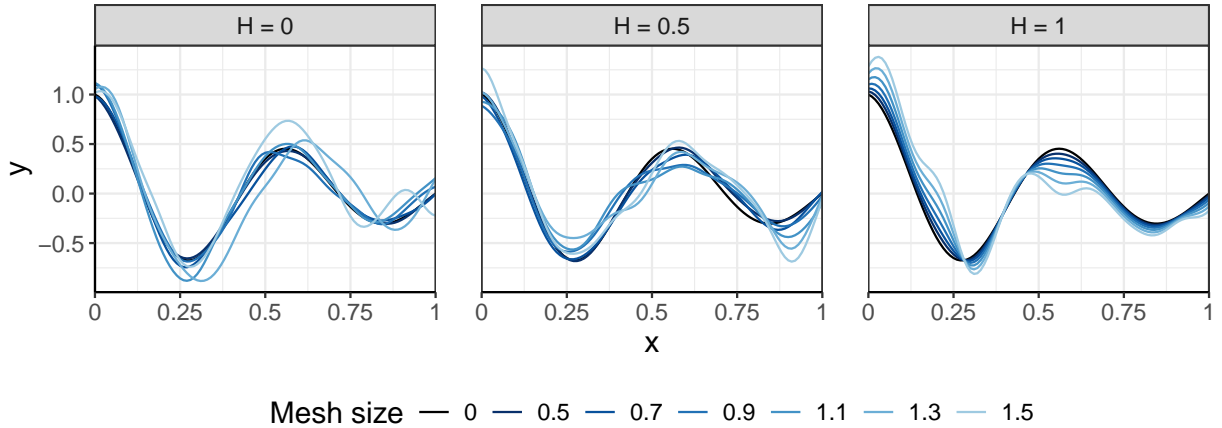


Figure 2: Realizations of the non-stationary model using the FBM kernel with three distinct values of H .

2.3 Illustration of the FBM Kernel’s Performance

We present examples from finite element simulations to illustrate the various possible output behaviors and demonstrate how our kernel function not only accurately interpolates the data but also achieves reliable extrapolation toward the true solution of the PDE.

We sample simulation data points in the whole domain $x \in [0, 1]$ with mesh sizes in $t \in [0.25/\sqrt{10}, 0.25]$ from the Poisson equation (in Section 5.1) with 2 different types of outputs (average or maximum value), and use the 3 different kernels to approximate the solution (i.e., $t = 0$). After fitting the surrogate model with each of the covariance functions, we predict the solution at $x = 0.25, 0.5, 0.75$. The results are displayed in Figure 3.

It can be observed that the proposed kernel effectively captures the dependency structure in relation to mesh size increments, whereas other kernels lack this capability. In particular, for the “Average” output, we observe a strong positive correlation in mesh size increments,

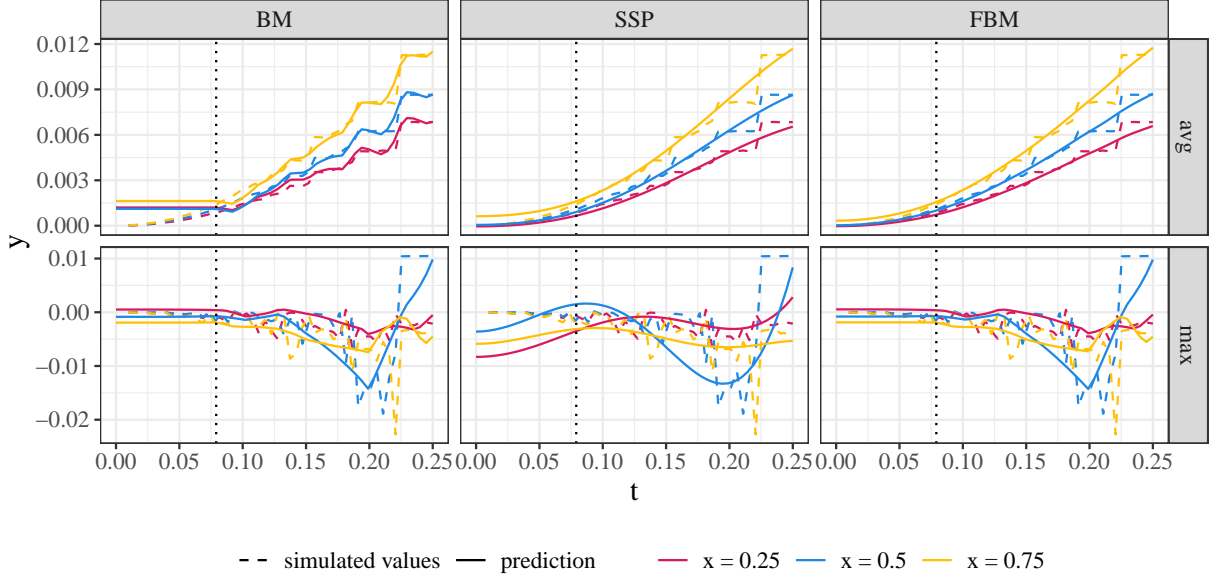


Figure 3: Results of FEA simulations on the Poisson's equation example with 2 different responses of interest: average (top) and maximum (bottom); the 3 columns correspond to the 3 different kernels considered here. The model is trained on mesh sizes $t \in [0.079, 0.25]$, and we extrapolate the results to the true solution $t = 0$. The vertical dashed line indicates the smallest mesh size value in the training data.

which the BM and SSP kernels fail to capture. This highlights the advantages of using the FBM for extrapolating when there is correlation between the increments.

Additionally, in this preliminary study, we observe that the dependency structure can be accurately estimated using our proposed covariance function through the parameter H , which is estimated as $H = 0.98$ for the “average” output, reflecting a highly correlated process, whereas for the “Maximum” output, we obtain an estimate of $H = 0.44$, indicating little to no dependency between the increments.

2.4 Statistical Inference

Suppose we have conducted n computer experiments at design locations $\mathbf{X}_n = (\mathbf{x}_1^T, \dots, \mathbf{x}_n^T)$ and mesh sizes $\mathbf{t}_n = (t_1, \dots, t_n)^T$, with the corresponding outputs $\mathbf{y}_n = (y_1, \dots, y_n)^T$, i.e., $y_i = y(\mathbf{x}_i, t_i)$.

To estimate the hyper-parameters $\{\boldsymbol{\beta}, \phi_1^2, \phi_2^2, \sigma_1^2, \sigma_2^2, H\}$, the Maximum Likelihood Estimation (MLE) is employed. First, we express the covariance function in (2) as

$K((\mathbf{x}_1, t_1), (\mathbf{x}_2, t_2)) = \sigma_1^2 K_0((\mathbf{x}_1, t_1), (\mathbf{x}_2, t_2))$ and introduce $\tau^2 = \frac{\sigma_2^2}{\sigma_1^2}$. Using the Restricted Maximum Likelihood Estimation (RMLE), we obtain the profile likelihood for $\boldsymbol{\beta}$ and σ_1^2 , and then estimate the remaining hyper-parameters (Stein, 1999; Santner et al., 2018). The profile likelihood to be maximized is

$$l(\boldsymbol{\theta}; \mathbf{y}_n) = \text{constant} - \frac{n-p}{2} \log \left\{ \mathbf{Z}^T \left(\mathbf{K}_{0,n}^{-1} - \mathbf{K}_{0,n}^{-1} \mathbf{F}_n \mathbf{P}_n^{-1} \mathbf{F}_n^T \mathbf{K}_{0,n}^{-1} \right) \mathbf{Z} \right\} - \frac{1}{2} \log |\mathbf{K}_{0,n}| - \frac{1}{2} \log |\mathbf{P}_n|$$

where $\mathbf{F}_n = (\mathbf{f}(\mathbf{x}_i, t_i)^T)_{1 \leq i \leq n}$, $\mathbf{Z} = (\mathbf{I} - \mathbf{F}_n (\mathbf{F}_n^T \mathbf{F}_n)^{-1} \mathbf{F}_n^T) \mathbf{y}_n$, $\mathbf{K}_{0,n} = (K_0((\mathbf{x}_i, t_i), (\mathbf{x}_j, t_j)))_{i,j}$ and $\mathbf{P}_n = \mathbf{F}_n^T \mathbf{K}_{0,n}^{-1} \mathbf{F}_n$, and p is the number of components in $\boldsymbol{\beta}$. The hyper-parameters $\{\phi_1^2, \phi_2^2, \tau^2, H\}$ can then be estimated by maximizing the likelihood $l(\boldsymbol{\theta}; \mathbf{y}_n)$, which can be achieved using a quasi-Newton optimization method (Byrd et al., 1995). The resulting MLEs for $\boldsymbol{\beta}$ and σ_1^2 are $\hat{\boldsymbol{\beta}} = (\mathbf{F}_n^T \mathbf{K}_{0,n}^{-1} \mathbf{F}_n)^{-1} \mathbf{F}_n^T \mathbf{K}_{0,n}^{-1} \mathbf{y}_n$ and $\hat{\sigma}_1^2 = \frac{(\mathbf{y}_n - \mathbf{F}_n \hat{\boldsymbol{\beta}})^T \mathbf{K}_{0,n}^{-1} (\mathbf{y}_n - \mathbf{F}_n \hat{\boldsymbol{\beta}})}{n-p}$, where $\mathbf{K}_{0,n}$ is calculated with the plug-in estimates $\{\hat{\phi}_1^2, \hat{\phi}_2^2, \hat{\tau}^2, \hat{H}\}$.

Although the number of hyperparameters is relatively low given the flexibility of the model, it can increase significantly as the dimension grows, making the optimization process computationally expensive. To address this, we derive closed-form expressions for the gradient of the log-likelihood in the Supplementary Materials. Compared to the fully Bayesian approach in Tuo et al. (2014), our method is more computationally efficient and avoids the need for informed priors. We will discuss parameter estimation in greater detail, as well as the need for experimental designs aimed at robust parameter estimation, in Section 3.2.

By the property of conditional normal distributions, the posterior distribution of $y(\mathbf{x}, t)$ given the observations \mathbf{y}_n follows a normal distribution with predictive mean and variance:

$$\begin{aligned} \mu_n(\mathbf{x}, t) &= \mathbf{f}(\mathbf{x}, t)^T \boldsymbol{\beta} + \mathbf{k}_n(\mathbf{x}, t)^T \mathbf{K}_n^{-1} (\mathbf{y}_n - \mathbf{F}_n \boldsymbol{\beta}), \\ \sigma_n^2(\mathbf{x}, t) &= K(\mathbf{x}, \mathbf{x}, t, t) - \mathbf{k}_n(\mathbf{x}, t)^T \mathbf{K}_n^{-1} \mathbf{k}_n(\mathbf{x}, t) + \gamma_n(\mathbf{x}, t)^T (\mathbf{F}_n^T \mathbf{K}_n^{-1} \mathbf{F}_n)^{-1} \gamma_n(\mathbf{x}, t), \end{aligned} \quad (3)$$

where $\mathbf{k}_n(\mathbf{x}, t)^T = (K((\mathbf{x}, t), (\mathbf{x}_i, t_i)))_{1 \leq i \leq n}$, $\mathbf{K}_n = (K((\mathbf{x}_i, t_i), (\mathbf{x}_j, t_j)))_{i,j}$, and $\gamma_n(\mathbf{x}, t) = (\mathbf{f}(\mathbf{x}, t) - \mathbf{F}_n^T \mathbf{K}_n^{-1} \mathbf{k}_n(\mathbf{x}, t))$. The hyper-parameters in the posterior distribution can be plugged in by their estimates.

From kriging theory (Cressie, 1993), this posterior predictive distribution is the Best Linear Unbiased Prediction (BLUP) for $y(\mathbf{x}, t)$. Unlike other multi-fidelity surrogate models that rely on auto-correlation models (Kennedy and O’Hagan, 2000; Le Gratiet and Cannamela, 2015; Heo and Sung, 2025), our surrogate model is capable of extrapolation, making predictions for the true solution at $t = 0$, while providing uncertainty quantification with the predictions.

3 Active Learning

In the context of computer simulations, where the need to carefully manage limited simulation resources intersects with the flexibility to choose design points without constraints, active learning methods have naturally gained popularity, particularly when combined with GP surrogate models (Rasmussen and Williams, 2006; Santner et al., 2018; Gramacy, 2020). In this work, we focus specifically on the objective of minimizing predictive error of the true solution.

3.1 Cost Adjusted IMSPE Reduction

We employ the Integrated Mean Squared Prediction Error (IMSPE) (Gramacy, 2020) as the foundation of our active learning criterion. IMSPE provides an intuitive tool for sequentially selecting points to minimize predictive error and has proven to be highly effective for complex GP surrogate models. The IMSPE measures the total posterior uncertainty in our prediction across the entire domain space. Since we are focused on predicting the true solution and not the error function over the entire mesh space \mathcal{T} , we integrate the Mean Squared Prediction Error (MSPE) only over the input space \mathcal{X} , with the prediction being made for $t = 0$. As our model specification implies that the prediction is unbiased, the MSPE is simply equal to the predictive variance $\sigma_n^2(\mathbf{x}, t)$ from (3). Given this, we define the IMSPE as

$$\text{IMSPE}(\mathbf{X}_n, \mathbf{t}_n) = \int_{\mathbf{x} \in \mathcal{X}} \sigma_n^2(\mathbf{x}, 0) d\mathbf{x} := I_n \tag{4}$$

Given the current design \mathbf{X}_n , our active learning objective is to find the next best

design location $(\mathbf{x}_{n+1}, t_{n+1})$ by minimizing $I_{n+1}(\mathbf{x}_{n+1}, t_{n+1}) := \text{IMSPE}(\mathbf{X}_{n+1}, \mathbf{t}_{n+1})$, where $\mathbf{X}_{n+1} = \{\mathbf{x}_1, \dots, \mathbf{x}_n, \mathbf{x}_{n+1}\}$ and $\mathbf{t}_{n+1} = \{t_1, \dots, t_n, t_{n+1}\}$ represent the combined set of n current design points and the new input location for the input parameters and mesh size. For any candidate point $(\tilde{\mathbf{x}}, \tilde{t})$, the following theorem shows that the IMSPE $I_{n+1}(\tilde{\mathbf{x}}, \tilde{t})$, can be written in a sequential manner, facilitating efficient computation when applied to an active learning method.

Theorem 1. *The IMSPE associated with an additional design point $(\tilde{\mathbf{x}}, \tilde{t})$ given the current design $(\mathbf{X}_n, \mathbf{t}_n)$ can be written in an iterative form as*

$$I_{n+1}(\tilde{\mathbf{x}}, \tilde{t}) = I_n - R_{n+1}(\tilde{\mathbf{x}}, \tilde{t}) \quad (5)$$

where $R_{n+1}(\tilde{\mathbf{x}}, \tilde{t})$, the IMSPE reduction, has a closed-form expression and can be computed with an $\mathcal{O}(n^2)$ cost complexity.

Proof. The proof, along with the closed-form expression of $R_{n+1}(\tilde{\mathbf{x}}, \tilde{t})$, can be found in the the Supplementary Materials. \square

A straightforward observation is that minimizing the IMSPE with an additional design point $(\tilde{\mathbf{x}}, \tilde{t})$ is equivalent to maximizing the IMSPE reduction, $R_{n+1}(\tilde{\mathbf{x}}, \tilde{t})$. We will, therefore, use $R_{n+1}(\tilde{\mathbf{x}}, \tilde{t})$ as the basis for our active learning criterion.

Because FEA simulations require managing the trade-off between accuracy and computational cost, our active learning method would be biased towards high-fidelity data points if we didn't account for the computational cost. Considering the simulation cost $C(t)$, our criterion selects the best next design point $(\mathbf{x}_{n+1}, t_{n+1})$ as

$$(\mathbf{x}_{n+1}, t_{n+1}) = \underset{(\tilde{\mathbf{x}}, \tilde{t}) \in \mathcal{X} \times \mathcal{T}}{\text{argmax}} \frac{R_{n+1}(\tilde{\mathbf{x}}, \tilde{t})}{C(\tilde{t})}.$$

Taking advantage of the continuous aspect of the domain on which the optimization is performed, we can use library-based numerical schemes to optimize our criterion. This is a novelty to the best of our knowledge, as other works have only explored active learning methods on a discrete set of candidate mesh sizes (Stroh et al., 2022; Sung et al., 2024; He

et al., 2017). An R package `MuFiMeshGP.AL` for the active learning method is available in an open repository and the Supplementary Materials.

Figure 4 illustrates the iterative process of selecting the optimal design point based on our active learning criterion. Starting from an initial design (left column), we fit our model and optimize our criterion to obtain the next best design point. A computer simulation is then run at this additional design point and added to our current design, after which we update the model. This process continues until the time budget is exhausted or a stopping criterion is met. Notably, the criterion is non-convex, requiring a multi-start optimization approach. To address this, we employ a simple multi-start procedure by selecting a set of m starting points with space-filling properties and good projection, such as the MaxPro design (Joseph et al., 2015), with the default value of m set to 20.

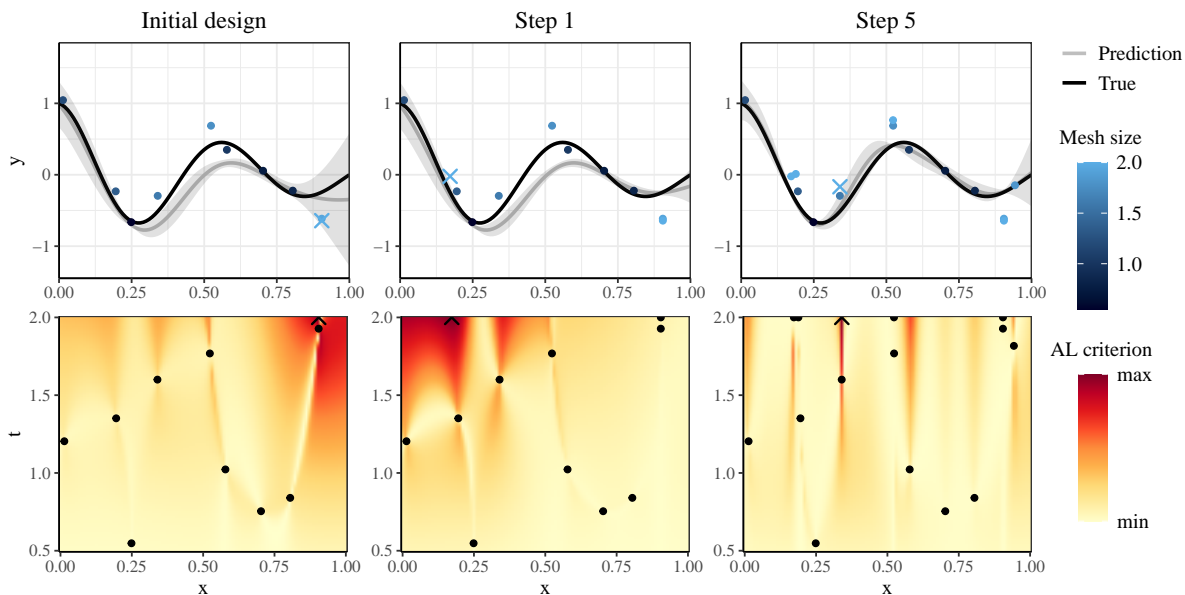


Figure 4: Prediction of our model (top), and active learning criterion surface (bottom). The points represent the current design locations (\bullet), and the best next design point according to the criterion (\times).

The simulation function in Figure 4 is $f(x) = e^{-1.4x} \cos(3.5\pi x) + t^2 \sin(40x)/10$, taken from Tuo et al. (2014), and represents a simulation where the increments are completely correlated (i.e., $H = 1$ in our model). Our active learning leverages this information by favoring data points that cost less but can inform the prediction as best as possible. In this case, the method selects data points that are close to previously sampled inputs, but with a

higher mesh size. The streaks of lighter color in the active learning criterion also reflect the highly correlated output, demonstrating that areas between closely spaced points can be interpolated by our model, yielding minimal additional information if new data points were sampled in those regions.

3.2 Initial Designs for Active Learning

In the example presented in the previous section, we observe somewhat surprising patterns in the behavior of our criterion. Depending on the estimated hyper-parameters $(\phi_1^2, \phi_2^2, \tau^2, H)$, the criterion can behave quite differently, highlighting how the active learning behavior is influenced by the estimation of the hyper-parameters from the initial design.

This issue was also raised by Song and Joseph (2025) in the context of screening designs for GP surrogate models, where they argue that space-filling designs are not necessarily the most optimal when used as initial designs for active learning methods. Indeed, while space-filling designs and active learning criteria are typically focused on improving the predictive performance of the model, they often do not explicitly account for uncertainty in parameter estimation, leading to a lack of certainty on the robustness of the subsequent parameter estimation. Despite the large body of literature on active learning methods and their performance, the problem of optimizing the initial design to improve overall predictive performance has been mostly reduced to the choice of initial sample size required to obtain good performances (Loeppky et al., 2009; Harari et al., 2018).

Our parameter estimation problem is driven by two main sources of uncertainties, both of which we believe can be addressed through better initial designs. The first arises from the inherent challenge in multi-fidelity simulations: the separation between the behavior of the real solution and the error function. In modeling terms, we need robust estimation of the parameter ϕ_2^2 that is able to differentiate it from ϕ_1^2 . Additionally, the parameter H from the FBM kernel significantly influences the behavior of our active learning method, making a good prior estimation crucial. These factors lead us to consider designs with a stacked structure to better capture the correlation between mesh sizes, thereby more accurately estimating H , as well as potentially a nested structure to better understand the behavior of

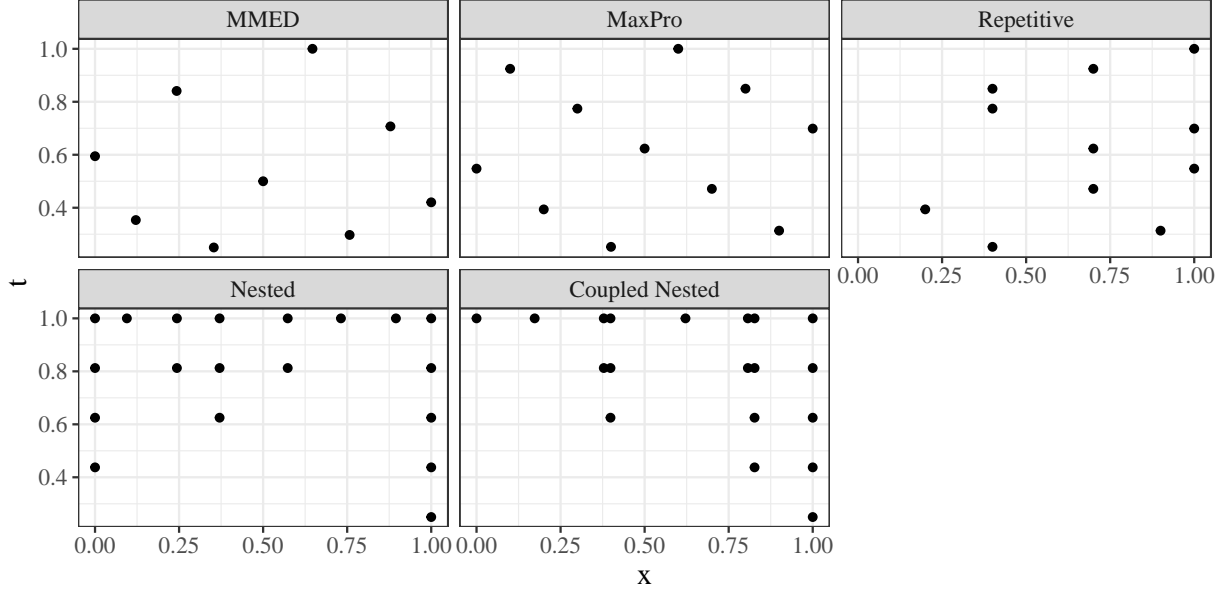


Figure 5: *Examples of different initial designs for the budget and cost function given in Section 4.*

the error function and improve the estimation of ϕ_2^2 .

We introduce three designs to address these parameter estimation challenges, and compare them with two existing designs that focus on space-filling and projection properties: the Maximum projection design (**MaxPro**) by Joseph et al. (2015), and the Multi-Mesh Experimental Design (**MMED**) by Shaowu Yuchi et al. (2023), an extension of the **MaxPro** design in which mesh size samples are chosen based on a weighted maximin criterion that accounts for computational cost.

The first experimental design is a straightforward extension of the **MaxPro** design, to which we add a constraint on the repetition of data points for each input space location. We call this design “Repetitive **MaxPro**” (**Repetitive**). The others two experimental designs are *nested* designs (Qian, 2009), meaning they consist of successive levels from low fidelity to high fidelity, with input space locations iteratively uniformly dropped at a rate of 2/3 at each fidelity level. The lowest fidelity design is either a **MaxPro** or space-filling design, and the mesh sizes are evenly distributed across the mesh size space. We consider two variants of this design: one that is purely space-filling (**Nested**), and another that includes coupled points (**Coupled Nested**), similar to the design in Zhu and Stein (2006), which incorporates uncertainty in the MSPE due to parameter estimation. All the designs are illustrated in

Figure 5.

4 Numerical Study

In this section, we first investigate the performance of different initial designs in terms of parameter estimation accuracy in Section 4.1. We then perform a more general simulation study in Section 4.2 to assess the performance of our active learning method with various initial designs and different non-stationary kernels.

The prediction performance is evaluated using two criteria: the root-mean-square error (RMSE) and continuous rank probability score (CRPS) (Gneiting and Raftery, 2007), as defined in the Supplementary Materials. The RMSE assesses the performance of the posterior mean, while the CRPS evaluates the posterior predictive distribution, providing a more comprehensive metric. For both RMSE and CRPS, lower values indicate superior model accuracy.

4.1 Evaluating the Experimental Initial Designs

Having defined different initial designs in Section 3.2, with the presumption that some may offer better parameter estimation, our goal here is to assess the robustness of the parameter estimation across these designs. Given that the parameter estimation is performed through MLE, using Fisher information provides a reliable method for evaluating parameter estimation performance.

We first assess the performance of the initial designs by comparing the Fisher information for the parameters $\phi_2^2 = 1, 10, 100$ and $H = 0.05, 0.5, 0.95$, covering a broad spectrum of behaviors. We then corroborate the parameter estimation performance through an empirical study, by constructing 10 simulations from our surrogate model for each parameter combination. The initial designs are constructed such that they all incur the same cost, using the cost function $C(t) = t^{-2}$. The results of these two studies are presented in the Supplementary Materials (Figures S1 and S2), along with further details on the calculation of the Fisher information.

These results demonstrate the superior performance of the nested designs in estimating ϕ_2^2 and H in most cases. Additionally, we observe that estimating H becomes more difficult as H decreases, a trend that corroborates the results of the Fisher information. On the other hand, the estimation of ϕ_2^2 from the non-nested designs does not significantly change as the true value of ϕ_2^2 varies, reflecting weak parameter estimation performance for those designs.

4.2 Simulation Study

We extend the simulation study presented in Section 4.1 by generating 9 sets of simulations with varying parameters $\phi_2^2 = 1, 10, 100$ and $H = 0.05, 0.5, 0.95$. Each set consists of 5 repetitions of 10 different functions simulated from our non-stationary model to ensure a sufficiently large sample. In this analysis, we compare the performance of the BM kernel against the FBM kernel and contrast the outcomes of using a one-shot design with those obtained through our active learning method. Additionally, we expand on the study in Section 4.1 by analyzing the impact of the different designs on the predictive performance of the active learning method, as well as the one-shot design approaches.

We define the range of possible mesh sizes as $[0.25, 1]$, with a total simulation budget of 96. This budget allows for 6 runs at the finest mesh size, where the cost function is given by $C(t) = t^{-2}$. The active learning procedure is performed with an initial budget of 48, allocated towards the initial design, corresponding to the sample designs from Figure 5. We also run a single fidelity surrogate model at mesh size $t = 0.25$ to gauge the performance of the different methods against the highest available fidelity level.

The resulting predictive performance in terms of CRPS for the different methods is summarized in Table 1. As expected, the single-fidelity surrogate models perform comparatively better when the underlying process is uncorrelated along the mesh size ($H = 0.5$) and the error function displays sharp fluctuations (higher ϕ_2^2). We clearly see that our FBM kernel performs much better than its BM counterpart when there is high correlation between mesh size increments ($H = 1$), reflecting the ability of the model to capture this information. Furthermore, the active learning method is able to leverage this

| Method | H = 0 | | | H = 0.5 | | | H = 1 | | |
|--------------------------|--------------|---------------|----------------|--------------|---------------|----------------|--------------|---------------|----------------|
| | $\phi_2^2=1$ | $\phi_2^2=10$ | $\phi_2^2=100$ | $\phi_2^2=1$ | $\phi_2^2=10$ | $\phi_2^2=100$ | $\phi_2^2=1$ | $\phi_2^2=10$ | $\phi_2^2=100$ |
| One-Shot BM - MMED | 0.036 | 0.096 | 0.140 | 0.051 | 0.086 | 0.153 | 0.049 | 0.108 | 0.169 |
| One-Shot BM - MaxPro | 0.055 | 0.059 | 0.055 | 0.054 | 0.042 | 0.055 | 0.032 | 0.050 | 0.058 |
| One-Shot FBM - MMED | 0.028 | 0.073 | 0.122 | 0.058 | 0.090 | 0.163 | 0.003 | 0.009 | 0.012 |
| One-Shot FBM - MaxPro | 0.043 | 0.054 | 0.050 | 0.054 | 0.047 | 0.055 | 0.005 | 0.008 | 0.045 |
| One-Shot Single Fidelity | 0.044 | 0.048 | 0.057 | 0.061 | 0.048 | 0.043 | 0.036 | 0.041 | 0.048 |
| AL BM - MMED | 0.030 | 0.059 | 0.065 | 0.042 | 0.048 | 0.066 | 0.023 | 0.050 | 0.083 |
| AL BM - MaxPro | 0.047 | 0.059 | 0.065 | 0.042 | 0.043 | 0.047 | 0.026 | 0.047 | 0.056 |
| AL FBM - MMED | 0.025 | 0.052 | 0.064 | 0.042 | 0.052 | 0.078 | 0.004 | 0.012 | 0.028 |
| AL FBM - MaxPro | 0.032 | 0.058 | 0.054 | 0.044 | 0.049 | 0.059 | 0.005 | 0.008 | 0.024 |
| AL FBM - Repetitive | 0.035 | 0.063 | 0.058 | 0.051 | 0.048 | 0.070 | 0.005 | 0.011 | 0.031 |
| AL FBM - Nested | 0.028 | 0.046 | 0.052 | 0.042 | 0.047 | 0.051 | 0.004 | 0.010 | 0.046 |
| AL FBM - Coupled Nested | 0.026 | 0.051 | 0.068 | 0.041 | 0.050 | 0.077 | 0.004 | 0.013 | 0.024 |
| AL Single Fidelity | 0.042 | 0.048 | 0.051 | 0.055 | 0.045 | 0.044 | 0.034 | 0.040 | 0.049 |

Table 1: *The estimated simulation CRPS for each method and each combination of ϕ_2^2 and H . The shading in the table indicates the performance of the method within its column, the darker indicating a higher CRPS and thus a worse predictive performance.*

information to achieve better performance, particularly in the challenging case of $\phi_2^2 = 100$. Figures S3, S4, and S5 in the Supplementary Materials provide the spread of results in terms of CRPS and parameter estimation across all parameter combinations.

The rest of the discussion focuses on comparing the performance of different experimental designs. Among the one-shot designs, the MaxPro design generally outperforms the MMED design, regardless of whether the FBM or BM kernel is used. For active learning, we observe that it generally outperforms its one-shot counterparts, although the one-shot FBM MaxPro method demonstrates competitive predictive performance. When using active learning, all initial designs combined with the FBM kernel yield strong predictive performance across most of the spectrum, with the repetitive design performing slightly worse than the others. These findings underscore the trade-off between accurate initial parameter estimation and a well-spread, space-filling design. Indeed, although the nested designs provide more robust parameter estimation early on, their weaker projection properties may initially hinder predictive performance. However, these effects appear to balance out over time, as we do not observe a significant difference in final predictive performance across different initial designs.

5 Case Studies

We assess the performance of our proposed surrogate model and active learning method through two case studies. In both of these studies we will compare the performance of our method with single-fidelity surrogate models as well with the stacking design method proposed by Sung et al. (2024). By using the single-fidelity surrogate models with several mesh sizes for comparison, we can showcase the variability in predictions depending on the selected mesh size and illustrate the trade-off between accuracy and computational cost.

In all the case studies, our mean regression functions, $\mathbf{f}_V(\mathbf{x})$, are Legendre 2nd degree polynomials on $[0, 1]$, supplemented with the interaction functions $((2x_i - 1)(2x_j - 1))_{1 \leq i < j \leq d}$. Additionally, we use $\mathbf{f}_Z(\mathbf{x}, t) = t^2$ to represent a possible trend effect in the underlying FEA simulations (Tuo et al., 2014).

5.1 Poisson’s Equation

We first use an elliptical PDE system to assess the performance of our method. The system of interest is modeled using Poisson’s equation on the square membrane $D = [0, 1] \times [0, 1]$,

$$\Delta u = (x^2 - 2\pi^2)e^{xz_1} \sin(\pi z_1) \sin(\pi z_2) + 2\pi x e^{xz_1} \cos(\pi z_1) \sin(\pi z_2), \quad (z_1, z_2) \in D,$$

where $u(z_1, z_2)$ is the solution of interest, $\Delta = \frac{\partial^2}{\partial z_1^2} + \frac{\partial^2}{\partial z_2^2}$ is the Laplace operator, and $x \in \mathcal{X} = [-1, 1]$ is our input parameter. A Dirichlet boundary condition $u = 0$ on the boundary ∂D is imposed on the system. Similar to Tuo et al. (2014) and Sung et al. (2024), this PDE is solved using FEA, specifically leveraging the PDE toolbox of MathWorks (2023) to create the geometry and mesh. The mesh size can be tuned continuously using this toolbox, although meshes generated for similar coarse mesh sizes tend to be very similar, leading to nearly identical output values, as illustrated in Figure 3.

We consider two different responses of interest for this study: the average over D and the maximum over D . The closed-form solution of this system given x is $u_x(z_1, z_2) = e^{xz_1} \sin(\pi z_1) \sin(\pi z_2)$, allowing us to derive an analytical expression for its average over D : $f_1(x) = \frac{2(e^x + 1)}{x^2 + \pi^2}$. For the maximum of the true solution over D , we determine it

numerically by optimizing u_x over D : $f_\infty(x) = \max_{(z_1, z_2) \in D} u_x(z_1, z_2)$. The cost function is again taken as $C(t) = t^{-2}$.

We conduct simulations with a total budget of 1500 and compare the performance of the surrogate model using the BM and FBM kernels, as well as our active learning method against one-shot designs. For the active learning approach, we allocate a budget of 500 toward the initial design, with a mesh size domain ranging between $\frac{0.25}{\sqrt{10}}$ and 0.25.

To benchmark our method, we compare it to single-fidelity predictions from one-shot designs as well as IMSPE-based active learning designs, using three different mesh sizes: $t = 0.06, 0.07, 0.08$. The active learning methods continue running until they reach the maximum budget of 1500. Given the high cost of simulating data points at small mesh sizes and the necessity of obtaining at least four data points, the single-fidelity methods begin active learning with a minimum of four data points.

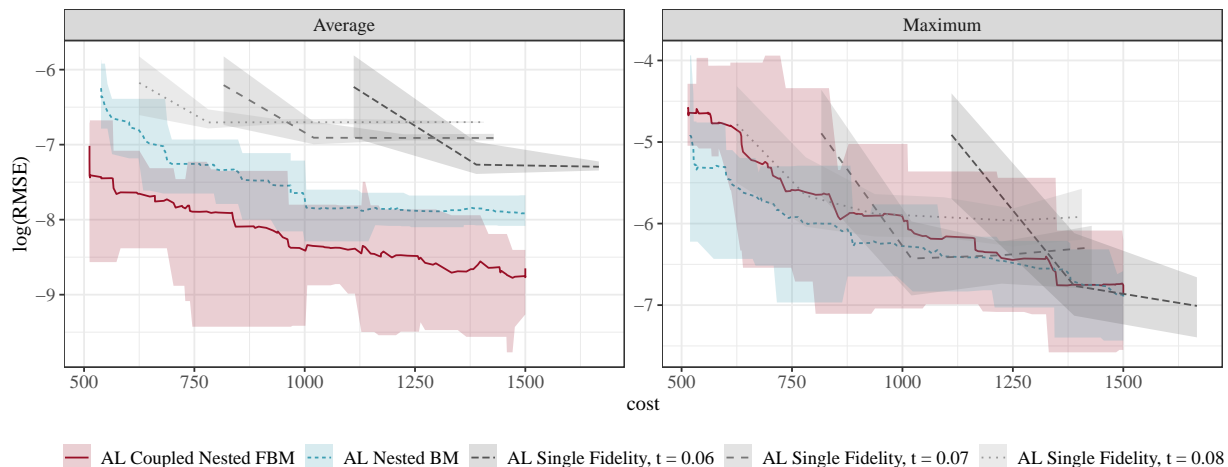


Figure 6: RMSE (in logarithmic scale) for the Poisson’s equation case study with respect to the simulation cost. Solid lines indicate the average over 10 repetitions, while shaded regions represent the range. The response of interest is the average (left) or the maximum (right) over the domain D .

Figure 6 presents the results of 10 simulations of active learning designs for each single-fidelity method, as well as the best-performing initial designs from the BM and FBM kernels. Recall that Figure 3 illustrates of the correlated structure of the two responses of interest, suggesting that our model is expected to perform particularly well under the “Average” response by leveraging this correlation. This is confirmed in the results, showing

that the FBM kernel significantly outperforms other methods, while the differences are less pronounced in the “Maximum” case. Nevertheless, our model remains highly competitive in this case, especially when compared to the highest-fidelity setting ($t = 0.06$), and provides a significant advantage over the single fidelity model because the single fidelity model requires selecting a mesh size prior to the start of the FEA simulation. If the chosen mesh size is too coarse, predictive accuracy suffers; if it is too fine, the surrogate model may fail to converge due to budget constraints, as evident in the right panel of Figure 6. In contrast, the multi-fidelity surrogate model offers the flexibility to incorporate various mesh sizes, enabling faster convergence within a fixed budget.

Additionally, we conduct the same simulations using one-shot designs and compare the prediction results from our surrogate model. We also compare with the stacking design method from Sung et al. (2024). All methods are allocated the same budget of 1500, although the highest-fidelity and stacking design methods exceed this limit, with an average final budget of 1667 and 1618, respectively.

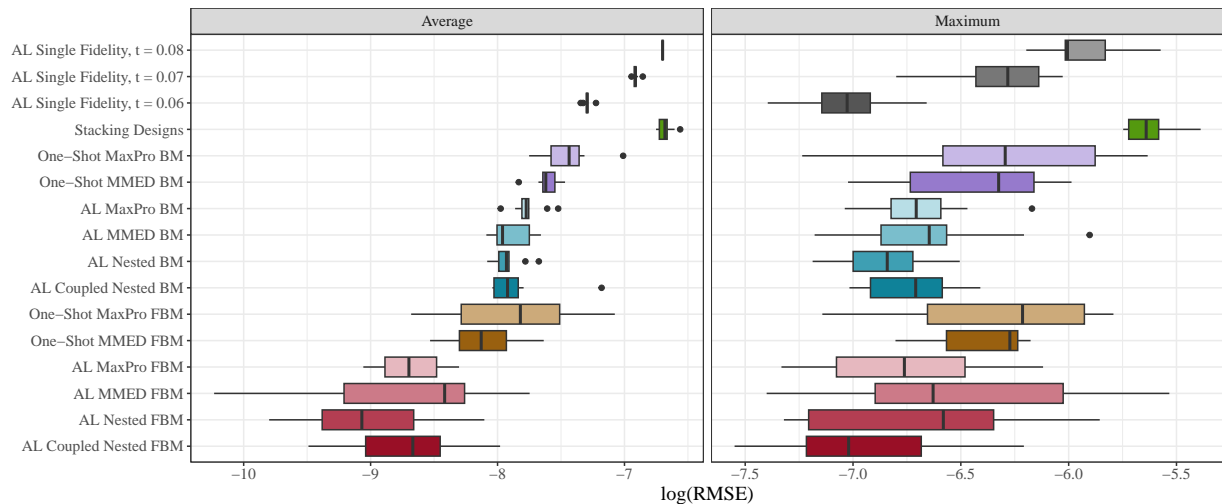


Figure 7: Boxplots of the final RMSE in logarithmic scale for the Poisson’s equation case study across 10 repetitions. The response of interest is the average (left) or the maximum (right) over the domain D .

Figure 7 shows the final RMSE (in logarithmic scale) after fully utilizing the allocated budget. The results demonstrates that the active learning method consistently outperforms its one-shot design counterparts, highlighting the superiority of active learning when it comes

to predictive performances. Additionally, we observe that the FBM kernel significantly outperforms the BM kernel in the “Average” case while remaining highly competitive in the “Maximum” case, showcasing both its adaptability and robustness. Furthermore, the estimation of the hyper-parameter H is shown in Figure S6, highlighting our model’s ability to accurately capture the correlation in the output, particularly when paired with the active learning method.

5.2 Stress Analysis of a Jet Engine Turbine Blade

Finally, we investigate the performance of our proposed model on a static structural analysis application for a jet turbine engine blade in steady-state operating condition. The turbine is a component of the jet engine, typically made from nickel alloys that resist extremely high temperatures, which needs to withstand high stress and deformations to avoid mechanical failure and friction between the tip of the blade and the turbine casing.

The effect of thermal stress and pressure of the surrounding gases on turbine blades can be solved with FEA as a static structural model. There are two input variables: the pressure load on the pressure (x_1), and suction (x_2) sides of the blade, both of which range from 0.25 to 0.75 MPa, i.e., $(x_1, x_2) \in \mathcal{X} = [0.25, 0.75]^2$. The response of interest in this problem is the displacement of the tip of the blade towards the casing, i.e., in the y-axis direction, to determine the pressure that the turbine can withstand before friction between the blade and the casing starts to appear (see Figure 1). FEA simulations are performed using the PDE toolbox of MathWorks (2023).

We conduct a preliminary study by running a sequence of simulations at the same input location but with decreasing mesh sizes, as shown in Figure 8. These simulations were performed on a High Performance Computing Center of the Institute for Cyber-Enabled Research (ICER) at MSU, utilizing up to 500GB of memory. This study has two purposes: first, to provide valuable insights for interpreting the results of this experiment, and second, to test how fine the mesh could be before encountering memory or computational time limitations. This helps us determine the appropriate mesh size for our test dataset. Following this preliminary study, we created a test dataset of 50 simulations sampled from

a MaxPro design on the input space, using a mesh size of $t = 0.001$, each of which took an average of 7500 seconds to complete. This test dataset is used as the true solution to evaluate the predictive performance. The output from the preliminary study, shown in Figure 8, highlights the trade-off between the computational cost of the simulation and its accuracy depending on the mesh size. As the mesh size increases, the computational time required for the FEA simulations grows substantially, while the response of interest converges quadratically to the true solution, as seen in the log-log convergence plot in Figure S7.

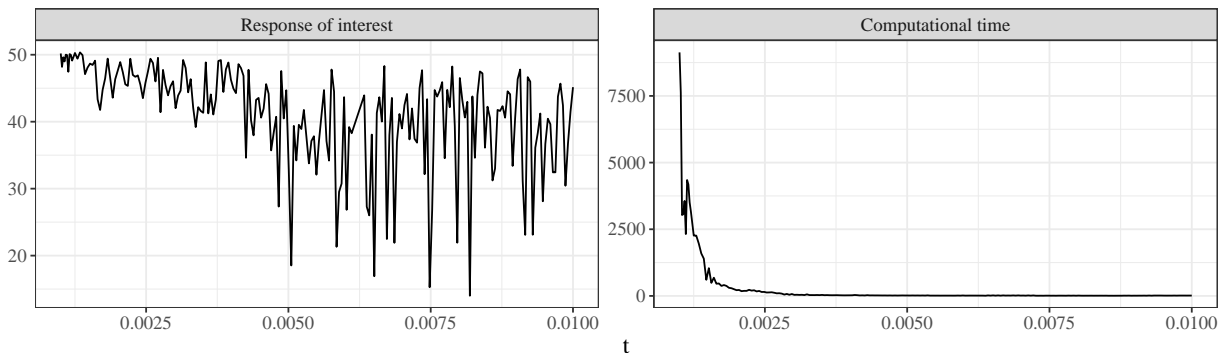


Figure 8: Results from the simulation on the jet engine turbine blade, with the response of interest (left) and the computational time (right) with respect to the mesh size.

For the cost function, we approximate it in the form $C(t) = bt^a + c$, where $a, b, c \in \mathbb{R}$ would be estimated from the initial design in a real-world study. However, for consistency across all simulations and to better align with a real-world setup, we ran a separate set of 20 simulations to estimate this function. The initial designs used by the active learning method include mesh sizes in the range $[0.0025, 0.01]$, and the active learning process maintains this range to stay within the interpolation region of the cost function. The single fidelity models with active learning used the following mesh sizes: $t = 0.0025, 0.003, 0.004, 0.005$. The total budget was set to 1500, with an initial budget of 350 allocated to the active learning methods. Additionally, we compare our method with the stacking design from Sung et al. (2024), using two different accuracy targets: $\varepsilon = 10, 15$, which result in average final budgets of 2828 and 1711, respectively.

The results of this study are summarized in Figures 9 and 10. Figure 9 displays the results

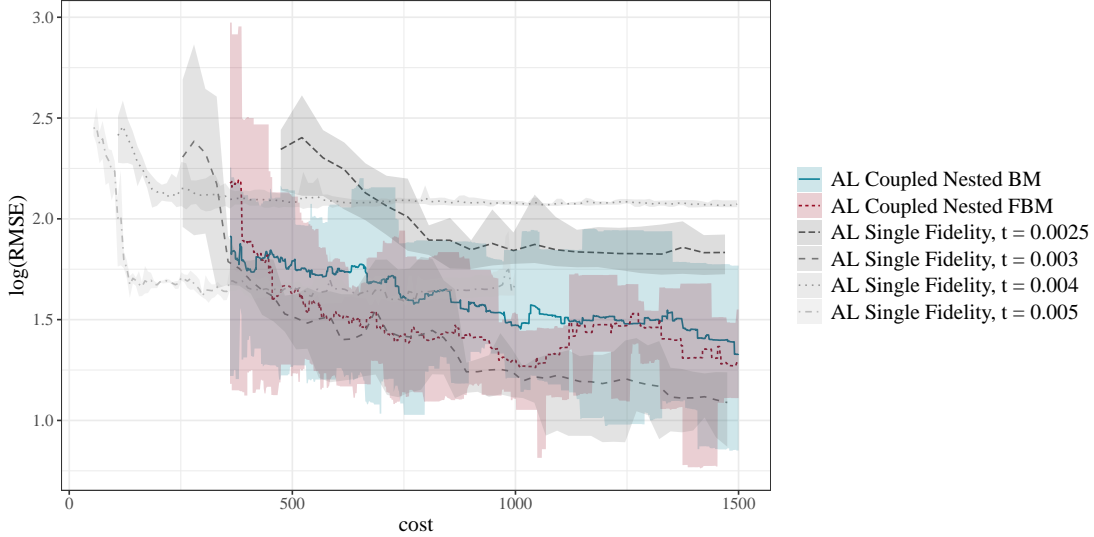


Figure 9: *RMSE (in logarithmic scale) for the jet engine turbine blade case study with respect to the simulation cost. Solid lines indicate the average over 5 repetitions, while shaded regions represent the range.*

with respect to the simulation cost, showing that the FBM kernel method outperforms the BM kernel method and most of the single-fidelity models. Additionally, we observe that choosing a finer mesh size does not always lead to better predictive performance, as the high variability of the response of interest comes into play (see Figure 8). This observation highlights the consistency and robustness of our model, particularly when compared to single-fidelity methods. When compared to stacking designs, our model’s predictive performance is superior, especially considering the higher budget required by the stacking designs approach. This can be attributed to the necessity of a nested structure in their method and the lack of extrapolation, which is essential for accurately predicting the true solution of the system.

Regarding the different options provided by our proposed model in terms of kernel choice (FBM or BM), design type (active learning or one-shot), and initial design selection, we find that, from Figure 10, the active learning method consistently delivers better predictions than its one-shot counterparts. The initial design choice does not seem to significantly affect the performance, although the `Coupled Nested` design performs slightly better on average. Additionally, we observe that the FBM kernel has a slight advantage over the BM kernel in this study. This further demonstrates the model’s ability to adapt to the underlying

structure of the outputs. The responsiveness of our model to the level of correlation in the outputs is illustrated in Figure S8, where we see that increments in mesh size are estimated to be negatively correlated ($H < 0.5$).

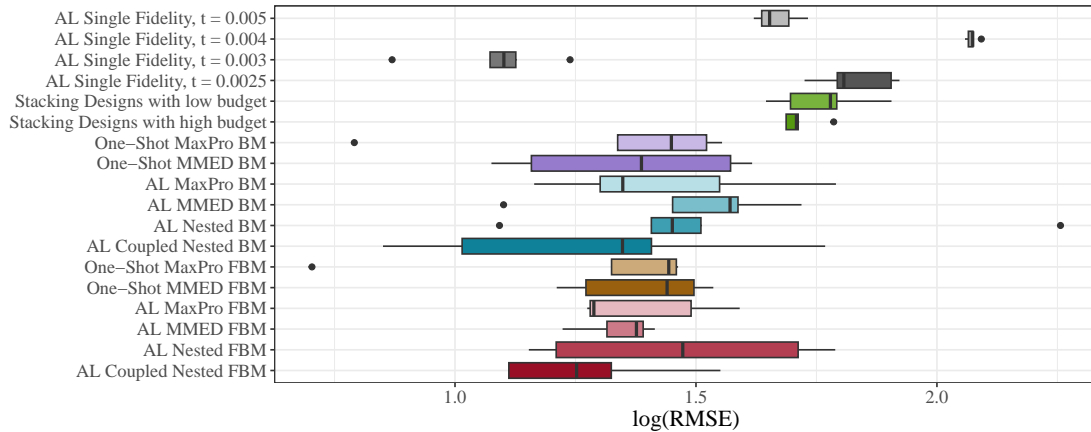


Figure 10: *Boxplots of the final RMSE in logarithmic scale for the jet engine turbine blade study across 5 repetitions.*

6 Conclusion

Surrogate modeling for multi-fidelity experiments, particularly in the context of FEA simulations with tunable mesh sizes, stands to benefit significantly from this new framework, which combines a novel kernel function that better captures the behavior of FEA outputs and an active learning method that can effectively leverage the continuous nature of the mesh size. Through simulation studies and experiments, we demonstrate that our active learning approach enhances the predictive performance of our model, while our proposed kernel offers greater flexibility and, in some cases, significantly outperforms other kernels.

We also highlighted the importance of the initial design in both the subsequent parameter estimation and the final predictive performance of the model. While the choice of initial design significantly impacts parameter estimation accuracy, its effect on the final prediction is less straightforward. The benefits of accurate parameter estimation must be balanced with the space-filling properties of the design. Further research is needed to explore this topic, particularly to account for varying sources of uncertainty, as discussed in Haaland et al.

(2018), which provides upper bounds for prediction errors due to numerical approximation and parameter estimation.

Additionally, it would be valuable to consider the transition costs between mesh configurations, particularly the potentially high cost of moving from a coarse to a dense mesh, to better reflect real-world constraints. The look-ahead approach proposed in Binois et al. (2019) could offer a promising direction for deciding whether to refine the mesh size or explore a new input location. We leave this as an avenue for future work.

Supplemental Materials Additional supporting materials can be found in Supplemental Materials, including the proof of Theorem 1, and the supporting figures for Sections 4 and 5. The R code and package for reproducing the results in Sections 4 and 5 are also provided.

References

- Barnett, S. (1979). *Matrix methods for engineers and scientists*. McGraw-Hill Book Co.
- Binois, M., Huang, J., Gramacy, R. B., and Ludkovski, M. (2019). Replication or exploration? sequential design for stochastic simulation experiments. *Technometrics*, 61(1):7–23.
- Brenner, S. C. and Scott, L. R. (2007). *The Mathematical Theory of Finite Element Methods (Third Edition)*. New York: Springer.
- Byrd, R. H., Lu, P., Nocedal, J., and Zhu, C. (1995). A limited memory algorithm for bound constrained optimization. *SIAM Journal on Scientific Computing*, 16(5):1190–1208.
- Cressie, N. (1993). *Statistics for Spatial Data*. John Wiley & Sons.
- Gneiting, T. and Raftery, A. E. (2007). Strictly proper scoring rules, prediction, and estimation. *Journal of the American Statistical Association*, 102(477):359–378.
- Gramacy, R. B. (2020). *Surrogates: Gaussian Process Modeling, Design, and Optimization for the Applied Sciences*. CRC press.

- Haaland, B., Wang, W., and Maheshwari, V. (2018). A framework for controlling sources of inaccuracy in Gaussian process emulation of deterministic computer experiments. *SIAM/ASA Journal on Uncertainty Quantification*, 6(2):497–521.
- Harari, O., Bingham, D., Dean, A., and Higdon, D. (2018). Computer experiments: Prediction accuracy, sample size and model complexity revisited. *Statistica Sinica*, 28(2):899–919.
- He, X., Tuo, R., and Wu, C. F. J. (2017). Optimization of multi-fidelity computer experiments via the EQIE criterion. *Technometrics*, 59(1):58–68.
- Heo, J. and Sung, C.-L. (2025). Active learning for a recursive non-additive emulator for multi-fidelity computer experiments. *Technometrics*, 67(1):58–72.
- Ji, Y., Mak, S., Soeder, D., Paquet, J., and Bass, S. A. (2024a). A graphical multi-fidelity Gaussian process model, with application to emulation of heavy-ion collisions. *Technometrics*, 66(2):267–281.
- Ji, Y., Yuchi, H. S., Soeder, D., Paquet, J.-F., Bass, S. A., Joseph, V. R., Wu, C. F. J., and Mak, S. (2024b). Conglomerate multi-fidelity Gaussian process modeling, with application to heavy-ion collisions. *SIAM/ASA Journal on Uncertainty Quantification*, 12(2):473–502.
- Joseph, V. R., Gul, E., and Ba, S. (2015). Maximum projection designs for computer experiments. *Biometrika*, 102(2):371–380.
- Kennedy, M. C. and O’Hagan, A. (2000). Predicting the output from a complex computer code when fast approximations are available. *Biometrika*, 87(1):1–13.
- Le Gratiet, L. (2013). Bayesian analysis of hierarchical multifidelity codes. *SIAM/ASA Journal on Uncertainty Quantification*, 1(1):244–269.
- Le Gratiet, L. and Cannamela, C. (2015). Cokriging-based sequential design strategies using fast cross-validation techniques for multi-fidelity computer codes. *Technometrics*, 57(3):418–427.

- Le Gratiet, L. and Garnier, J. (2014). Recursive co-kriging model for design of computer experiments with multiple levels of fidelity. *International Journal for Uncertainty Quantification*, 4(5):365–386.
- Loeppky, J. L., Sacks, J., and Welch, W. J. (2009). Choosing the sample size of a computer experiment: A practical guide. *Technometrics*, 51(4):366–376.
- Mak, S., Sung, C.-L., Wang, X., Yeh, S.-T., Chang, Y.-H., Joseph, V. R., Yang, V., and Wu, C. F. J. (2018). An efficient surrogate model for emulation and physics extraction of large eddy simulations. *Journal of the American Statistical Association*, 113(524):1443–1456.
- MathWorks, I. (2023). Partial differential equation toolbox version: 9.14 (r2023a).
- Perdikaris, P., Raissi, M., Damianou, A., Lawrence, N. D., and Karniadakis, G. E. (2017). Nonlinear information fusion algorithms for data-efficient multi-fidelity modelling. *Proceedings of the Royal Society A: Mathematical, Physical and Engineering Sciences*, 473(2198):20160751.
- Petersen, K. B. and Pedersen, M. S. (2008). The matrix cookbook. Version 20081110.
- Qian, P. Z. G. (2009). Nested Latin hypercube designs. *Biometrika*, 96(4):957–970.
- Qian, P. Z. G. and Wu, C. F. J. (2008). Bayesian hierarchical modeling for integrating low-accuracy and high-accuracy experiments. *Technometrics*, 50(2):192–204.
- Qian, Z., Seepersad, C. C., Joseph, V. R., Allen, J. K., and Wu, C. F. J. (2006). Building surrogate models based on detailed and approximate simulations. *Journal of Mechanical Design*, 128(4):668–677.
- Rasmussen, C. E. and Williams, C. K. (2006). *Gaussian Processes for Machine Learning*. Cambridge, MA: MIT Press.
- Santner, T. J., Williams, B. J., and Notz, W. I. (2018). *The Design and Analysis of Computer Experiments*. Springer New York.

- Shaowu Yuchi, H., Roshan Joseph, V., and Wu, C. F. J. (2023). Design and analysis of multifidelity finite element simulations. *Journal of Mechanical Design*, 145(6):061703.
- Sherman, J. and Morrison, W. J. (1950). Adjustment of an inverse matrix corresponding to a change in one element of a given matrix. *The Annals of Mathematical Statistics*, 21(1):124–127.
- Song, D. and Joseph, V. R. (2025). Efficient active learning strategies for computer experiments.
- Stein, M. L. (1999). *Interpolation of Spatial Data: Some Theory for Kriging*. Springer Science & Business Media.
- Stroh, R., Bect, J., Demeyer, S., Fischer, N., Marquis, D., and Vazquez, E. (2022). Sequential design of multi-fidelity computer experiments: maximizing the rate of stepwise uncertainty reduction. *Technometrics*, 64(2):199–209.
- Sung, C.-L., Ji, Y., Mak, S., Wang, W., and Tang, T. (2024). Stacking designs: Designing multifidelity computer experiments with target predictive accuracy. *SIAM/ASA Journal on Uncertainty Quantification*, 12(1):157–181.
- Tuo, R., Wu, C. F. J., and Yu, D. (2014). Surrogate modeling of computer experiments with different mesh densities. *Technometrics*, 56(3):372–380.
- Zhu, Z. and Stein, M. L. (2006). Spatial sampling design for prediction with estimated parameters. *Journal of Agricultural, Biological, and Environmental Statistics*, 11(1):24–44.

Supplementary Material for "Active Learning for Finite Element Simulations with Adaptive Non-Stationary Kernel Function"

A Proof of Theorem 1

Following from Binois et al. (2019), we can obtain that the IMSPE can take a closed-form expression, avoiding the computational burden of evaluating the integral over the whole domain.

Lemma 2. *Let $\mathbf{W}_n = (w(\mathbf{x}_i, \mathbf{x}_j))_{i,j}$ be a $N \times N$ matrix with*

$$w(\mathbf{x}_i, \mathbf{x}_j) = \int_{\mathbf{x} \in \mathcal{X}} K((\mathbf{x}_i, 0), (\mathbf{x}, 0))K((\mathbf{x}_j, 0), (\mathbf{x}, 0))d\mathbf{x}.$$

Let $E = \int_{\mathbf{x} \in \mathcal{X}} K((\mathbf{x}, 0), (\mathbf{x}, 0))d\mathbf{x}$, let $\mathbf{G} = (g_{i,j})_{i,j}$ be a $p \times p$ matrix such that $g_{i,j} = \int_{\mathbf{x} \in \mathcal{X}} f_i(\mathbf{x}, 0)f_j(\mathbf{x}, 0)d\mathbf{x}$, and let $\mathbf{H}_n = (h_j(\mathbf{x}_i))_{i,j}$ be a $n \times p$ matrix such that $h_j(\mathbf{x}_i) = \int_{\mathbf{x} \in \mathcal{X}} k_n((\mathbf{x}_i, 0), (\mathbf{x}, 0))f_j(\mathbf{x}, 0)d\mathbf{x}$. Then,

$$I_n = E - \text{tr}(\mathbf{K}_n^{-1}\mathbf{W}_n) + \text{tr}(\mathbf{M}_n\mathbf{W}_n) + \text{tr}((\mathbf{F}_n^T\mathbf{K}_n^{-1}\mathbf{F}_n)^{-1}\mathbf{G}) - 2.\text{tr}(\mathbf{P}_n\mathbf{H}_n) \quad (6)$$

where $\mathbf{M}_n = \mathbf{K}_n^{-1}\mathbf{F}_n(\mathbf{F}_n^T\mathbf{K}_n^{-1}\mathbf{F}_n)^{-1}\mathbf{F}_n^T\mathbf{K}_n^{-1}$, and $\mathbf{P}_n = (\mathbf{F}_n^T\mathbf{K}_n^{-1}\mathbf{F}_n)^{-1}\mathbf{F}_n^T\mathbf{K}_n^{-1}$.

Proof. Observing that

$$\begin{aligned}
I_n &= \int_{\mathbf{x} \in \mathcal{X}} \sigma_n^2(\mathbf{x}, 0) d\mathbf{x} \\
&= \int_{\mathbf{x} \in \mathcal{X}} K((\mathbf{x}, 0), (\mathbf{x}, 0)) - \mathbf{k}_n(\mathbf{x}, 0)^T \mathbf{K}_n^{-1} \mathbf{k}_n(\mathbf{x}, 0) + (\boldsymbol{\gamma}_n(\mathbf{x}, 0))^T (\mathbf{F}_n^T \mathbf{K}_n^{-1} \mathbf{F}_n)^{-1} \boldsymbol{\gamma}_n(\mathbf{x}, 0) d\mathbf{x} \\
&= \mathbb{E} [K((X, 0), (X, 0))] - \mathbb{E} [\mathbf{k}_n(X, 0)^T \mathbf{K}_n^{-1} \mathbf{k}_n(X, 0)] + \mathbb{E} [(\boldsymbol{\gamma}_n(X, 0))^T (\mathbf{F}_n^T \mathbf{K}_n^{-1} \mathbf{F}_n)^{-1} \boldsymbol{\gamma}_n(X, 0)]
\end{aligned}$$

where X is uniformly sampled on \mathcal{X} .

Since $K((X, 0), (X, 0)) = \sigma_1^2 R_{\phi_1}(X, X) = \sigma_1^2$, we can set $E = \mathbb{E} [K((X, 0), (X, 0))]$ aside since it will stay constant.

Binois et al. (2019) cleverly observe that

$$\mathbb{E} [\mathbf{k}_n(X, 0)^T \mathbf{K}_n^{-1} \mathbf{k}_n(X, 0)] = \text{tr} (\mathbb{E} [\mathbf{K}_n^{-1} \mathbf{k}_n(X, 0) \mathbf{k}_n(X, 0)^T]) = \mathbb{E} [\mathbf{K}_n^{-1} (\mathbf{M} + \mathbf{m} \mathbf{m}^T)]$$

where $\mathbf{M} = \text{Cov}(\mathbf{k}_n(X, 0), \mathbf{k}_n(X, 0))$, and $\mathbf{m} = \mathbb{E} [\mathbf{k}_n(X, 0)]$. Observing that $\mathbf{W}_n = \mathbf{M} + \mathbf{m} \mathbf{m}^T$ yields the first part of the proof.

We can extend this to the term $\mathbb{E} [(\boldsymbol{\gamma}_n(X, 0))^T (\mathbf{F}_n^T \mathbf{K}_n^{-1} \mathbf{F}_n)^{-1} \boldsymbol{\gamma}_n(X, 0)]$ by first using that $\boldsymbol{\gamma}_n(X, 0) = (\mathbf{f}(X, 0) - \mathbf{F}_n^T \mathbf{K}_n^{-1} \mathbf{k}_n(X, 0))$ to obtain

$$\begin{aligned}
\mathbb{E} [(\boldsymbol{\gamma}_n(X, 0))^T (\mathbf{F}_n^T \mathbf{K}_n^{-1} \mathbf{F}_n)^{-1} \boldsymbol{\gamma}_n(X, 0)] &= \mathbb{E} [\mathbf{f}(X, 0)^T (\mathbf{F}_n^T \mathbf{K}_n^{-1} \mathbf{F}_n)^{-1} \mathbf{f}(X, 0)] \\
&\quad + \mathbb{E} [\mathbf{k}_n(X, 0)^T \mathbf{K}_n^{-1} \mathbf{F}_n (\mathbf{F}_n^T \mathbf{K}_n^{-1} \mathbf{F}_n)^{-1} \mathbf{F}_n^T \mathbf{K}_n^{-1} \mathbf{k}_n(X, 0)] - \\
&\quad 2 \cdot \mathbb{E} [\mathbf{f}(X, 0)^T (\mathbf{F}_n^T \mathbf{K}_n^{-1} \mathbf{F}_n)^{-1} \mathbf{F}_n^T \mathbf{K}_n^{-1} \mathbf{k}_n(X, 0)]
\end{aligned}$$

We can observe that

$$\begin{aligned}
\mathbb{E} [\mathbf{f}(X, 0)^T (\mathbf{F}_n^T \mathbf{K}_n^{-1} \mathbf{F}_n)^{-1} \mathbf{f}(X, 0)] &= \text{tr} ((\mathbf{F}_n^T \mathbf{K}_n^{-1} \mathbf{F}_n)^{-1} \mathbb{E} [\mathbf{f}(X, 0) \mathbf{f}(X, 0)^T]) \\
&= \text{tr} ((\mathbf{F}_n^T \mathbf{K}_n^{-1} \mathbf{F}_n)^{-1} \mathbf{G})
\end{aligned}$$

$$\begin{aligned}
\mathbb{E} [\mathbf{k}_n(X, 0)^T \mathbf{K}_n^{-1} \mathbf{F}_n (\mathbf{F}_n^T \mathbf{K}_n^{-1} \mathbf{F}_n)^{-1} \mathbf{F}_n^T \mathbf{K}_n^{-1} \mathbf{k}_n(X, 0)] \\
&= \text{tr} (\mathbf{K}_n^{-1} \mathbf{F}_n (\mathbf{F}_n^T \mathbf{K}_n^{-1} \mathbf{F}_n)^{-1} \mathbf{F}_n^T \mathbf{K}_n^{-1} \mathbb{E} [\mathbf{k}_n(X, 0) \mathbf{k}_n(X, 0)^T]) \\
&= \text{tr} (\mathbf{M}_n \mathbf{W}_n)
\end{aligned}$$

$$\begin{aligned}
\mathbb{E} [\mathbf{f}(X, 0)^T (\mathbf{F}_n^T \mathbf{K}_n^{-1} \mathbf{F}_n)^{-1} \mathbf{F}_n^T \mathbf{K}_n^{-1} \mathbf{k}_n(X, 0)] &= \text{tr} ((\mathbf{F}_n^T \mathbf{K}_n^{-1} \mathbf{F}_n)^{-1} \mathbf{F}_n^T \mathbf{K}_n^{-1} \mathbb{E} [\mathbf{k}_n(X, 0) \mathbf{f}(X, 0)^T]) \\
&= \text{tr} (\mathbf{P}_n \mathbf{H}_n)
\end{aligned}$$

The final form (A.1) follows from the three equations above. \square

Fixing the first n design points, we obtain the following forms for \mathbf{K}_{n+1} and \mathbf{W}_{n+1} using the new design point candidate $(\tilde{\mathbf{x}}, \tilde{t})$.

$$\mathbf{K}_{n+1} = \begin{bmatrix} \mathbf{K}_n & \mathbf{k}_n(\tilde{\mathbf{x}}, \tilde{t}) \\ \mathbf{k}_n(\tilde{\mathbf{x}}, \tilde{t})^T & K((\tilde{\mathbf{x}}, \tilde{t}), (\tilde{\mathbf{x}}, \tilde{t})) \end{bmatrix}, \quad \mathbf{W}_{n+1} = \begin{bmatrix} \mathbf{W}_n & \mathbf{w}(\tilde{\mathbf{x}}) \\ \mathbf{w}(\tilde{\mathbf{x}})^T & w(\tilde{\mathbf{x}}, \tilde{\mathbf{x}}) \end{bmatrix}$$

where $\mathbf{w}(\tilde{\mathbf{x}}) = (w(\tilde{\mathbf{x}}, \mathbf{x}_i))_{1 \leq i \leq N}$.

The partitioned matrix inverse (Barnett, 1979) gives,

$$\mathbf{K}_{n+1}^{-1} = \begin{bmatrix} \mathbf{K}_n^{-1} + \sigma_n^2(\tilde{\mathbf{x}}, \tilde{t}) \mathbf{a}(\tilde{\mathbf{x}}, \tilde{t}) \mathbf{a}(\tilde{\mathbf{x}}, \tilde{t})^T & \mathbf{a}(\tilde{\mathbf{x}}, \tilde{t}) \\ \mathbf{a}(\tilde{\mathbf{x}}, \tilde{t})^T & \sigma_n^2(\tilde{\mathbf{x}}, \tilde{t})^{-1} \end{bmatrix}$$

where $\mathbf{a}(\tilde{\mathbf{x}}, \tilde{t}) = -\sigma_n^2(\tilde{\mathbf{x}}, \tilde{t})^{-1} \mathbf{K}_n^{-1} \mathbf{k}_n(\tilde{\mathbf{x}}, \tilde{t})$

Following the framework from Binois et al. (2019), we use the decomposition $\text{tr}(\mathbf{K}_n^{-1} \mathbf{W}_n) = \mathbf{1}^T (\mathbf{K}_n^{-1} \odot \mathbf{W}_n) \mathbf{1}$, where \odot represents the Hadamard (element-wise) product for matrices.

Combining these two results gives us

$$\begin{aligned}
\text{tr}(\mathbf{K}_{n+1}^{-1} \mathbf{W}_{n+1}) &= \mathbf{1}^T (\mathbf{K}_{n+1}^{-1} \odot \mathbf{W}_{n+1}) \mathbf{1} \\
&= \mathbf{1}^T (\mathbf{K}_n^{-1} \odot \mathbf{W}_n) \mathbf{1} + \sigma_n^2(\tilde{\mathbf{x}}, \tilde{t}) \mathbf{a}(\tilde{\mathbf{x}}, \tilde{t})^T \mathbf{W}_n \mathbf{a}(\tilde{\mathbf{x}}, \tilde{t}) + 2\mathbf{w}(\tilde{\mathbf{x}})^T \mathbf{a}(\tilde{\mathbf{x}}, \tilde{t}) + \sigma_n^2(\tilde{\mathbf{x}}, \tilde{t})^{-1} w(\tilde{\mathbf{x}}, \tilde{\mathbf{x}}) \\
&= \text{tr}(\mathbf{K}_n^{-1} \mathbf{W}_n) + \sigma_n^2(\tilde{\mathbf{x}}, \tilde{t}) \mathbf{a}(\tilde{\mathbf{x}}, \tilde{t})^T \mathbf{W}_n \mathbf{a}(\tilde{\mathbf{x}}, \tilde{t}) + 2\mathbf{w}(\tilde{\mathbf{x}})^T \mathbf{a}(\tilde{\mathbf{x}}, \tilde{t}) + \sigma_n^2(\tilde{\mathbf{x}}, \tilde{t})^{-1} w(\tilde{\mathbf{x}}, \tilde{\mathbf{x}})
\end{aligned} \tag{7}$$

We can also obtain the following partitioned forms for \mathbf{F}_{n+1} and \mathbf{H}_{n+1} ,

$$\mathbf{F}_{n+1} = \begin{bmatrix} \mathbf{F}_n \\ \mathbf{f}(\tilde{\mathbf{x}}, \tilde{t})^T \end{bmatrix}, \quad \mathbf{H}_{n+1} = \begin{bmatrix} \mathbf{H}_n \\ \mathbf{h}(\tilde{\mathbf{x}})^T \end{bmatrix}$$

where $\mathbf{h}(\tilde{\mathbf{x}}) = (h_j(\tilde{\mathbf{x}}))_{1 \leq j \leq p}$.

We use partitioned matrix equations to obtain that

$$\mathbf{F}_{n+1}^T \mathbf{K}_{n+1}^{-1} \mathbf{F}_{n+1} = \mathbf{F}_n^T \mathbf{K}_n^{-1} \mathbf{F}_n + \mathbf{v} \mathbf{v}^T \quad (8)$$

where $\mathbf{v} = \tilde{\sigma}_n(\tilde{\mathbf{x}}, \tilde{t}) \mathbf{F}_n^T \mathbf{a}(\tilde{\mathbf{x}}, \tilde{t}) + (\tilde{\sigma}_n(\tilde{\mathbf{x}}, \tilde{t}))^{-1} f(\tilde{\mathbf{x}}, \tilde{t})$, and $\tilde{\sigma}_n^2(\tilde{\mathbf{x}}, \tilde{t}) = K((\tilde{\mathbf{x}}, \tilde{t}), (\tilde{\mathbf{x}}, \tilde{t})) - \mathbf{k}_n(\tilde{\mathbf{x}}, \tilde{t})^T \mathbf{K}_n^{-1} \mathbf{k}_n(\tilde{\mathbf{x}}, \tilde{t})$.

The Sherman-Morrison formula (Sherman and Morrison, 1950) on (8) leads to

$$(\mathbf{F}_{n+1}^T \mathbf{K}_{n+1}^{-1} \mathbf{F}_{n+1})^{-1} = (\mathbf{F}_n^T \mathbf{K}_n^{-1} \mathbf{F}_n)^{-1} - \mathbf{B}_n \quad (9)$$

where $\mathbf{B}_n = \frac{(\mathbf{F}_n^T \mathbf{K}_n^{-1} \mathbf{F}_n)^{-1} \mathbf{v} \mathbf{v}^T (\mathbf{F}_n^T \mathbf{K}_n^{-1} \mathbf{F}_n)^{-1}}{1 + \mathbf{v}^T (\mathbf{F}_n^T \mathbf{K}_n^{-1} \mathbf{F}_n)^{-1} \mathbf{v}}$.

Additionally, we can observe that

$$\mathbf{K}_{n+1}^{-1} \mathbf{F}_{n+1} = \begin{bmatrix} \mathbf{K}_n^{-1} \mathbf{F}_n \\ \mathbf{0}_p^T \end{bmatrix} + \mathbf{U}_n \quad (10)$$

where $\mathbf{U}_n = \begin{bmatrix} \mathbf{S}_n \\ \mathbf{T}_n \end{bmatrix} = \begin{bmatrix} \tilde{\sigma}_n^2(\tilde{\mathbf{x}}, \tilde{t}) \mathbf{a}(\tilde{\mathbf{x}}, \tilde{t}) \mathbf{a}(\tilde{\mathbf{x}}, \tilde{t})^T \mathbf{F}_n + \mathbf{a}(\tilde{\mathbf{x}}, \tilde{t}) f(\tilde{\mathbf{x}}, \tilde{t})^T \\ \mathbf{a}(\tilde{\mathbf{x}}, \tilde{t})^T \mathbf{F}_n + (\tilde{\sigma}_n^2(\tilde{\mathbf{x}}, \tilde{t}))^{-1} f(\tilde{\mathbf{x}}, \tilde{t})^T \end{bmatrix}$.

Using equations (9) and (10), we can obtain the following results:

$$\begin{aligned} \mathbf{M}_{n+1} = & \begin{bmatrix} \mathbf{M}_n - \mathbf{K}_n^{-1} \mathbf{F}_n \mathbf{B}_n \mathbf{F}_n^T \mathbf{K}_n^{-1} & \mathbf{0}_n \\ \mathbf{0}_n^T & 0 \end{bmatrix} + \begin{bmatrix} \mathbf{K}_n^{-1} \mathbf{F}_n ((\mathbf{F}_n^T \mathbf{K}_n^{-1} \mathbf{F}_n)^{-1} - \mathbf{B}_n) \mathbf{U}_n^T \\ \mathbf{0}_{n+1}^T \end{bmatrix} \\ & + \begin{bmatrix} \mathbf{K}_n^{-1} \mathbf{F}_n ((\mathbf{F}_n^T \mathbf{K}_n^{-1} \mathbf{F}_n)^{-1} - \mathbf{B}_n) \mathbf{U}_n^T \\ \mathbf{0}_{n+1}^T \end{bmatrix}^T + \mathbf{U}_n ((\mathbf{F}_n^T \mathbf{K}_n^{-1} \mathbf{F}_n)^{-1} - \mathbf{B}_n) \mathbf{U}_n^T \end{aligned} \quad (11)$$

$$\mathbf{P}_{n+1} = \begin{bmatrix} \mathbf{P}_n & \mathbf{0}_p \end{bmatrix} - \begin{bmatrix} \mathbf{B}_n \mathbf{F}_n^T \mathbf{K}_n^{-1} & \mathbf{0}_p \end{bmatrix} + ((\mathbf{F}_n^T \mathbf{K}_n^{-1} \mathbf{F}_n)^{-1} - \mathbf{B}_n) \mathbf{U}_n^T \quad (12)$$

From all these derivations, and using the results from Lemma 1, it follows that

$$\begin{aligned} I_{n+1}(\tilde{\mathbf{x}}, \tilde{t}) &= E - \text{tr}(\mathbf{K}_{n+1}^{-1} \mathbf{W}_{n+1}) + \text{tr}(\mathbf{M}_{n+1} \mathbf{W}_{n+1}) + \text{tr}((\mathbf{F}_{n+1}^T \mathbf{K}_{n+1}^{-1} \mathbf{F}_{n+1})^{-1} \mathbf{G}) - 2 \cdot \text{tr}(\mathbf{P}_{n+1} \mathbf{H}_{n+1}) \\ &= E - \text{tr}(\mathbf{K}_n^{-1} \mathbf{W}_n) + \text{tr}(\mathbf{M}_n \mathbf{W}_n) + \text{tr}((\mathbf{F}_n^T \mathbf{K}_n^{-1} \mathbf{F}_n)^{-1} \mathbf{G}) - 2 \cdot \text{tr}(\mathbf{P}_n \mathbf{H}_n) - R_{n+1}(\tilde{\mathbf{x}}, \tilde{t}) \\ &= I_n - R_{n+1}(\tilde{\mathbf{x}}, \tilde{t}) \end{aligned} \quad (13)$$

To fully develop $R_{n+1}(\tilde{\mathbf{x}}, \tilde{t})$, we write it as a sum of 4 elements :

$$R_{n+1}(\tilde{\mathbf{x}}, \tilde{t}) = R_{n+1}^{(1)}(\tilde{\mathbf{x}}, \tilde{t}) + R_{n+1}^{(2)}(\tilde{\mathbf{x}}, \tilde{t}) + R_{n+1}^{(3)}(\tilde{\mathbf{x}}, \tilde{t}) + R_{n+1}^{(4)}(\tilde{\mathbf{x}}, \tilde{t})$$

such that:

$$\begin{aligned} R_{n+1}^{(1)}(\tilde{\mathbf{x}}, \tilde{t}) &= \text{tr}(\mathbf{K}_{n+1}^{-1} \mathbf{W}_{n+1}) - \text{tr}(\mathbf{K}_n^{-1} \mathbf{W}_n) \\ &= \tilde{\sigma}_n^2(\tilde{\mathbf{x}}, \tilde{t}) \mathbf{a}(\tilde{\mathbf{x}}, \tilde{t})^T \mathbf{W}_n \mathbf{a}(\tilde{\mathbf{x}}, \tilde{t}) + 2 \mathbf{w}(\tilde{\mathbf{x}})^T \mathbf{a}(\tilde{\mathbf{x}}, \tilde{t}) + \tilde{\sigma}_n^2(\tilde{\mathbf{x}}, \tilde{t})^{-1} w(\tilde{\mathbf{x}}, \tilde{t}) \end{aligned}$$

$$\begin{aligned}
R_{n+1}^{(2)}(\tilde{\mathbf{x}}, \tilde{t}) &= \text{tr}(\mathbf{M}_{n+1} \mathbf{W}_{n+1}) - \text{tr}(\mathbf{M}_n \mathbf{W}_n) \\
&= \text{tr}(\mathbf{K}_n^{-1} \mathbf{F}_n \mathbf{B}_n \mathbf{F}_n^T \mathbf{K}_n^{-1} \mathbf{W}_n) - \text{tr}((\mathbf{S}_n + 2\mathbf{K}_n^{-1} \mathbf{F}_n) ((\mathbf{F}_n^T \mathbf{K}_n^{-1} \mathbf{F}_n)^{-1} - \mathbf{B}_n) \mathbf{S}_n^T \mathbf{W}_n) \\
&\quad - 2 \cdot \mathbf{T}_n ((\mathbf{F}_n^T \mathbf{K}_n^{-1} \mathbf{F}_n)^{-1} - \mathbf{B}_n) (\mathbf{S}_n^T + \mathbf{F}_n^T \mathbf{K}_n^{-1}) \mathbf{w}(\tilde{\mathbf{x}}) - \mathbf{T}_n ((\mathbf{F}_n^T \mathbf{K}_n^{-1} \mathbf{F}_n)^{-1} - \mathbf{B}_n) \mathbf{T}_n^T w(\tilde{\mathbf{x}}, \tilde{\mathbf{x}})
\end{aligned}$$

$$\begin{aligned}
R_{n+1}^{(3)}(\tilde{\mathbf{x}}, \tilde{t}) &= \text{tr}((\mathbf{F}_{n+1}^T \mathbf{K}_{n+1}^{-1} \mathbf{F}_{n+1})^{-1} \mathbf{G}) - \text{tr}((\mathbf{F}_n^T \mathbf{K}_n^{-1} \mathbf{F}_n)^{-1} \mathbf{G}) \\
&= \text{tr}(\mathbf{B}_n \mathbf{G})
\end{aligned}$$

$$\begin{aligned}
R_{n+1}^{(4)}(\tilde{\mathbf{x}}, \tilde{t}) &= -2 \left[\text{tr}(\mathbf{P}_{n+1} \mathbf{H}_{n+1}) - \text{tr}(\mathbf{P}_n \mathbf{H}_n) \right] \\
&= -2 \left[\text{tr}(\mathbf{B}_n \mathbf{F}_n^T \mathbf{K}_n^{-1} \mathbf{H}_n) \right. \\
&\quad \left. - \text{tr}(((\mathbf{F}_n^T \mathbf{K}_n^{-1} \mathbf{F}_n)^{-1} - \mathbf{B}_n) \mathbf{S}_n^T \mathbf{H}_n) - \mathbf{h}(\tilde{\mathbf{x}})^T ((\mathbf{F}_n^T \mathbf{K}_n^{-1} \mathbf{F}_n)^{-1} - \mathbf{B}_n) \mathbf{T}_n^T \right]
\end{aligned}$$

More importantly, we can observe that given that the hyper-parameters remain the same, \mathbf{K}_n^{-1} and \mathbf{W}_n do not need to be reevaluated, leading to significant improvements in terms of computational efficiency. The cost complexity is then only $\mathcal{O}(n^2)$, considering that for all the above calculations, we can use the faster form $\text{tr}(AB) = \mathbf{1}^T(A \odot B)\mathbf{1}$, for A, B symmetric matrices.

B Gradients of the log-likelihood

The first step in deriving the gradient of the log-likelihood is to derive the gradient of $\mathbf{K}_{0,n}$ with respect of all its hyper-parameters. We remind the reader of the log-likelihood,

$$l(\boldsymbol{\theta}; \mathbf{Y}) \propto -\frac{n-p}{2} \log \left\{ \mathbf{Z}^T (\mathbf{K}_{0,n}^{-1} - \mathbf{K}_{0,n}^{-1} \mathbf{F}_n \mathbf{P}_n^{-1} \mathbf{F}_n^T \mathbf{K}_{0,n}^{-1}) \mathbf{Z} \right\} - \frac{1}{2} \log |\mathbf{K}_{0,n}| - \frac{1}{2} \log |\mathbf{P}_n| \quad (14)$$

with $\mathbf{P}_n = \mathbf{F}_n^T \mathbf{K}_{0,n}^{-1} \mathbf{F}_n$.

Assuming a square exponential correlation function on the input space, we easily find the following

$$\frac{\partial R_{\phi_i}(\mathbf{x}_1, \mathbf{x}_2)}{\partial \phi_i} = (x_{1,i} - x_{2,i})^2 R_{\phi_i}(\mathbf{x}_1, \mathbf{x}_2) \quad (15)$$

We can then obtain the gradient of K_H with respect to H ,

$$\begin{aligned} \frac{\partial K_H(t_1, t_2)}{\partial H} = & \left[\frac{l}{H} \frac{\log(t_1)t_1^{2H} + \log(t_2)t_2^{2H} - \log(|t_1 - t_2|)|t_1 - t_2|^{2H}}{t_1^{2H} + t_2^{2H} - |t_1 - t_2|^{2H}} \right. \\ & \left. - \frac{l}{2H^2} \log\left(\frac{t_1^{2H} + t_2^{2H} - |t_1 - t_2|^{2H}}{2}\right) \right] \cdot K_H(t_1, t_2) \end{aligned} \quad (16)$$

It is then straightforward to obtain the gradient of $\mathbf{K}_{0,n}$ with respect to all the hyper-parameters.

From here, we can obtain the gradients for \mathbf{P}_n for any hyper-parameter θ by carefully performing matrix calculus (Petersen and Pedersen, 2008),

$$\frac{\partial \mathbf{K}_{0,n}^{-1}}{\partial \theta} = -\mathbf{K}_{0,n}^{-1} \frac{\partial \mathbf{K}_{0,n}}{\partial \theta} \mathbf{K}_{0,n}^{-1} \quad (17)$$

$$\frac{\partial \mathbf{P}_n}{\partial \theta} = \mathbf{F}_n^T \frac{\partial \mathbf{K}_{0,n}^{-1}}{\partial \theta} \mathbf{F}_n \quad (18)$$

We can additionally find the gradients for the log of the determinants

$$\frac{\partial \log |\mathbf{K}_{0,n}|}{\partial \theta} = \text{tr} \left(\mathbf{K}_{0,n}^{-1} \frac{\partial \mathbf{K}_{0,n}}{\partial \theta} \right) \quad (19)$$

$$\frac{\partial \log |\mathbf{P}_n|}{\partial \theta} = \text{tr} \left(\mathbf{P}_n^{-1} \frac{\partial \mathbf{P}_n}{\partial \theta} \right) \quad (20)$$

Finally, for any hyper-parameter, we obtain the following gradient of the log likelihood

$$\begin{aligned}
\frac{\partial l(\boldsymbol{\theta}; \mathbf{Y})}{\partial \boldsymbol{\theta}} &= -\frac{1}{2} \text{tr} \left(\mathbf{K}_{0,n}^{-1} \frac{\partial \mathbf{K}_{0,n}}{\partial \boldsymbol{\theta}} \right) - \frac{1}{2} \text{tr} \left(\mathbf{P}_n^{-1} \frac{\partial \mathbf{P}_n}{\partial \boldsymbol{\theta}} \right) \\
&\quad - \frac{n-p}{2} \cdot \frac{\mathbf{Z}^T \left(2 \cdot \frac{\partial \mathbf{K}_{0,n}^{-1}}{\partial \boldsymbol{\theta}} \mathbf{F}_n \mathbf{P}_n^{-1} \mathbf{F}_n^T \mathbf{K}_{0,n}^{-1} + \mathbf{K}_{0,n}^{-1} \mathbf{F}_n \frac{\partial \mathbf{P}_n}{\partial \boldsymbol{\theta}} \mathbf{F}_n^T \mathbf{K}_{0,n}^{-1} \right) \mathbf{Z} - \mathbf{Z}^T \frac{\partial \mathbf{K}_{0,n}^{-1}}{\partial \boldsymbol{\theta}} \mathbf{Z}}{\mathbf{Z}^T (\mathbf{K}_{0,n}^{-1} - \mathbf{K}_{0,n}^{-1} \mathbf{F}_n \mathbf{P}_n^{-1} \mathbf{F}_n^T \mathbf{K}_{0,n}^{-1}) \mathbf{Z}}
\end{aligned} \tag{21}$$

C Closed form expressions for the square exponential correlation function

The closed-form expression for \mathbf{W}_n can be found in Binois et al. (2019).

We will detail the expressions of $g_{i,j}$ and $h_j(\mathbf{x}_i)$ in the cases $f_j(\mathbf{x}, t) = 1$, $f_j(\mathbf{x}, t) = x_{k_j}$, $f_j(\mathbf{x}, t) = x_{k_j}^2$. If using other orthogonal such as Legendre polynomials, one can simply use linear combinations of those results. We will use $\mathcal{D} = [0, 1]^d$ for simplicity.

First, we derive the term $h_j(\mathbf{x}_i)$:

We first define 3 integrals,

$$\begin{aligned}
I_{1,k}^{(i)} &:= \int_0^1 \sigma_1^2 \exp(-\phi_k^2(x - x_{i,k})^2) dx = \sigma_1^2 \frac{\sqrt{\pi}}{\phi_k} \left[\Phi(\sqrt{2}\phi_k(1 - x_{i,k})) - \Phi(-\sqrt{2}\phi_k x_{i,k}) \right] \\
I_{2,k}^{(i)} &= \sigma_1^2 \int_0^1 2\phi_k^2(x - x_{i,k}) \exp(-\phi_k^2(x - x_{i,k})^2) dx = \sigma_1^2 \left[\exp(-\phi_k^2 x_{i,k}^2) - \exp(-\phi_k^2(1 - x_{i,k})^2) \right] \\
I_{3,k}^{(i)} &= \sigma_1^2 \int_0^1 2\phi_k^2(x - x_{i,k})^2 \exp(-\phi_k^2(x - x_{i,k})^2) dx \\
&= \sigma_1^2 \left(\left[-(x - x_{i,k}) \exp(-\phi_k^2(x - x_{i,k})^2) \right]_0^1 + \int_0^1 \exp(-\phi_k^2(x - x_{i,k})^2) dx \right) \\
&= \sigma_1^2 \left[-x_{i,k} \exp(-\phi_k^2 x_{i,k}^2) - (1 - x_{i,k}) \exp(-\phi_k^2(1 - x_{i,k})^2) \right] + I_{1,k}^{(i)}
\end{aligned}$$

- For $f_j(\mathbf{x}, t) = 1$, and with $\mathbf{x}_i = (\mathbf{x}_{i,1}, \dots, \mathbf{x}_{i,p})^T$,

$$h_j(\mathbf{x}_i) = \int_{\mathbf{x} \in \mathcal{D}} k((\mathbf{x}_i, 0), (\mathbf{x}, 0)) f_j(\mathbf{x}, 0) d\mathbf{x} = \prod_{k=1}^d \int_0^1 \sigma_1^2 \exp(-\phi_k^2(x - x_{i,k})^2) dx = \prod_{k=1}^d I_{1,k}^{(i)}$$

- For $f_j(\mathbf{x}, t) = x_{k_j}$,

$$\begin{aligned}
h_j(\mathbf{x}_i) &= \int_{\mathbf{x} \in \mathcal{D}} k((\mathbf{x}_i, 0), (\mathbf{x}, 0)) f_j(\mathbf{x}, 0) d\mathbf{x} = \int_{\mathbf{x} \in \mathcal{D}} k((\mathbf{x}_i, 0), (\mathbf{x}, 0)) x_{k_j} d\mathbf{x} \\
&= \left(\sigma_1^2 \int_0^1 y \exp(-\phi_{k_j}^2 (y - x_{i,k_j})^2) dy \right) \left(\prod_{k \neq k_j} \int_0^1 \sigma_1^2 \exp(-\phi_k^2 (x - x_{i,k})^2) dx \right) \\
&= \left(\frac{I_{2,k_j}^{(i)}}{2\phi_{k_j}^2} + x_{i,k_j} I_{1,k_j}^{(i)} \right) \left(\prod_{k \neq k_j} I_{1,k}^{(i)} \right)
\end{aligned}$$

- For $f_j(\mathbf{x}, t) = x_{k_j}^2$,

$$\begin{aligned}
h_j(\mathbf{x}_i) &= \int_{\mathbf{x} \in \mathcal{D}} k((\mathbf{x}_i, 0), (\mathbf{x}, 0)) f_j(\mathbf{x}, 0) d\mathbf{x} = \int_{\mathbf{x} \in \mathcal{D}} k((\mathbf{x}_i, 0), (\mathbf{x}, 0)) x_{k_j}^2 d\mathbf{x} \\
&= \left(\sigma_1^2 \int_0^1 y^2 \exp(-\phi_{k_j}^2 (y - x_{i,k_j})^2) dy \right) \left(\prod_{k \neq k_j} \int_0^1 \sigma_1^2 \exp(-\phi_k^2 (x - x_{i,k})^2) dx \right) \\
&= \left(\frac{I_{3,k_j}^{(i)}}{2\phi_{k_j}^2} + x_{i,k_j} \frac{I_{2,k_j}^{(i)}}{\phi_{k_j}^2} + x_{i,k_j}^2 I_{1,k_j}^{(i)} \right) \left(\prod_{k \neq k_j} I_{1,k}^{(i)} \right)
\end{aligned}$$

- For $f_j(\mathbf{x}, t) = x_{k_{j_1}} x_{k_{j_2}}$,

$$\begin{aligned}
h_j(\mathbf{x}_i) &= \int_{\mathbf{x} \in \mathcal{D}} k((\mathbf{x}_i, 0), (\mathbf{x}, 0)) f_j(\mathbf{x}, 0) d\mathbf{x} = \int_{\mathbf{x} \in \mathcal{D}} k((\mathbf{x}_i, 0), (\mathbf{x}, 0)) x_{k_{j_1}} x_{k_{j_2}} d\mathbf{x} \\
&= \left(\sigma_1^2 \int_0^1 y \exp(-\phi_{k_{j_1}}^2 (y - x_{i,k_{j_1}})^2) dy \right) \times \\
&\quad \left(\sigma_1^2 \int_0^1 y \exp(-\phi_{k_{j_2}}^2 (y - x_{i,k_{j_2}})^2) dy \right) \left(\prod_{k \notin \{k_{j_1}, k_{j_2}\}} \int_0^1 \sigma_1^2 \exp(-\phi_k^2 (x - x_{i,k})^2) dx \right) \\
&= \left(\frac{I_{2,k_{j_1}}^{(i)}}{2\phi_{k_{j_1}}^2} + x_{i,k_{j_1}} I_{1,k_{j_1}}^{(i)} \right) \left(\frac{I_{2,k_{j_2}}^{(i)}}{2\phi_{k_{j_2}}^2} + x_{i,k_{j_2}} I_{1,k_{j_2}}^{(i)} \right) \left(\prod_{k \notin \{k_{j_1}, k_{j_2}\}} I_{1,k}^{(i)} \right)
\end{aligned}$$

Then, we derive the closed form expressions for $g_{i,j}$:

- For $f_i(\mathbf{x}, t) = 1$ and $f_j(\mathbf{x}, t) = 1$, then $g_{i,j} = 1$
- For $f_i(\mathbf{x}, t) = 1$ and $f_j(\mathbf{x}, t) = x_{k_j}$, then $g_{i,j} = \frac{1}{2}$

- For $f_i(\mathbf{x}, t) = 1$ and $f_j(\mathbf{x}, t) = x_{k_j}^2$, then $g_{i,j} = \frac{1}{3}$
- For $f_i(\mathbf{x}, t) = x_{k_i}$ and $f_j(\mathbf{x}, t) = x_{k_j}$ with $i \neq j$, then $g_{i,j} = \frac{1}{4}$
- For $f_i(\mathbf{x}, t) = x_{k_i}$ and $f_j(\mathbf{x}, t) = x_{k_j}$ with $i = j$, then $g_{i,j} = \frac{1}{3}$
- For $f_i(\mathbf{x}, t) = x_{k_i}$ and $f_j(\mathbf{x}, t) = x_{k_j}^2$ with $i \neq j$, then $g_{i,j} = \frac{1}{6}$
- For $f_i(\mathbf{x}, t) = x_{k_i}$ and $f_j(\mathbf{x}, t) = x_{k_j}^2$ with $i = j$, then $g_{i,j} = \frac{1}{4}$
- For $f_i(\mathbf{x}, t) = x_{k_i}^2$ and $f_j(\mathbf{x}, t) = x_{k_j}^2$ with $i \neq j$, then $g_{i,j} = \frac{1}{9}$
- For $f_i(\mathbf{x}, t) = x_{k_i}^2$ and $f_j(\mathbf{x}, t) = x_{k_j}^2$ with $i = j$, then $g_{i,j} = \frac{1}{5}$
- For $f_i(\mathbf{x}, t) = x_{k_{i_1}} x_{k_{i_2}}$ and $f_j(\mathbf{x}, t) = 1$ with $i_1 \neq i_2$, then $g_{i,j} = \frac{1}{4}$
- For $f_i(\mathbf{x}, t) = x_{k_{i_1}} x_{k_{i_2}}$ and $f_j(\mathbf{x}, t) = x_{k_j}$ with i_1, i_2, j all distinct, then $g_{i,j} = \frac{1}{8}$
- For $f_i(\mathbf{x}, t) = x_{k_{i_1}} x_{k_{i_2}}$ and $f_j(\mathbf{x}, t) = x_{k_j}$ with $i_1 \neq i_2 = j_1$, then $g_{i,j} = \frac{1}{6}$
- For $f_i(\mathbf{x}, t) = x_{k_{i_1}} x_{k_{i_2}}$ and $f_j(\mathbf{x}, t) = x_{k_j}^2$ with i_1, i_2, j all distinct, then $g_{i,j} = \frac{1}{12}$
- For $f_i(\mathbf{x}, t) = x_{k_{i_1}} x_{k_{i_2}}$ and $f_j(\mathbf{x}, t) = x_{k_j}^2$ with $i_1 \neq i_2 = j_1$, then $g_{i,j} = \frac{1}{8}$
- For $f_i(\mathbf{x}, t) = x_{k_{i_1}} x_{k_{i_2}}$ and $f_j(\mathbf{x}, t) = x_{k_{j_1}} x_{k_{j_2}}$ with i_1, i_2, j_1, j_2 all distinct, then $g_{i,j} = \frac{1}{16}$
- For $f_i(\mathbf{x}, t) = x_{k_{i_1}} x_{k_{i_2}}$ and $f_j(\mathbf{x}, t) = x_{k_{j_1}} x_{k_{j_2}}$ with $i_1 \neq i_2 = j_1$, and $j_2 \neq j_1$, then $g_{i,j} = \frac{1}{12}$
- For $f_i(\mathbf{x}, t) = x_{k_{i_1}} x_{k_{i_2}}$ and $f_j(\mathbf{x}, t) = x_{k_{j_1}} x_{k_{j_2}}$ with $j_1 = i_1 \neq i_2 = j_2$, then $g_{i,j} = \frac{1}{9}$

D Definitions of RMSE and CRPS

For testing the results from a Gaussian process with posterior mean function μ and posterior standard deviation σ against the true function f and with testing data points $\mathbf{X}^{\text{test}} = (\mathbf{x}_i^{\text{test}})_{1 \leq i \leq n_{\text{test}}}$, we can define the RMSE and CRPS as follows Gneiting and Raftery (2007),

$$\text{RMSE} = \left(\sum_i^{n_{\text{test}}} \frac{(f(\mathbf{x}_i^{\text{test}}) - \mu(\mathbf{x}_i^{\text{test}}))^2}{n_{\text{test}}} \right)^{1/2}$$

$$\text{CRPS} = \frac{1}{n_{\text{test}}} \sum_i^{n_{\text{test}}} \sigma(\mathbf{x}_i^{\text{test}}) \left[\frac{1}{\sqrt{\pi}} - 2\phi(z(\mathbf{x}_i^{\text{test}})) - z(\mathbf{x}_i^{\text{test}}) (2\Phi(z(\mathbf{x}_i^{\text{test}})) - 1) \right]$$

where $z(\mathbf{x}_i^{\text{test}}) = \frac{f(\mathbf{x}_i^{\text{test}}) - \mu(\mathbf{x}_i^{\text{test}})}{\sigma(\mathbf{x}_i^{\text{test}})}$, and with ϕ and Φ denoting respectively the probability density function and cumulative distribution function of a standard normal distribution.

E Supporting materials for Section 4

For a GP with constant mean and covariance kernel $K_{\boldsymbol{\theta}}$, the Fisher information for parameter θ_i takes the simple form

$$F_{\theta_i} = \mathcal{I}_{i,i}(\boldsymbol{\theta}) = \frac{1}{2} \text{tr} \left(\mathbf{K}_{\boldsymbol{\theta}}^{-1} \frac{\partial \mathbf{K}_{\boldsymbol{\theta}}}{\partial \theta_i} \mathbf{K}_{\boldsymbol{\theta}}^{-1} \frac{\partial \mathbf{K}_{\boldsymbol{\theta}}}{\partial \theta_j} \right) \quad (22)$$

where we can use the results from Section B to obtain the closed form expressions of the Fisher information matrix components.

This section provides the supporting figures for Section 4, including the Fisher information for parameters ϕ_2^2 and H across each of their plausible domains (Figure S1). For each parameter, we study the Fisher information with 3 different underlying value of H or ϕ_2^2 , respectively, to observe the possible interaction between the parameter values and the Fisher information. It also includes the results of the parameter estimation study from Section 4.1 (Figure S2), and the CRPS, and parameter estimation results from Section 4.2 (Figure S3, S4, S5).

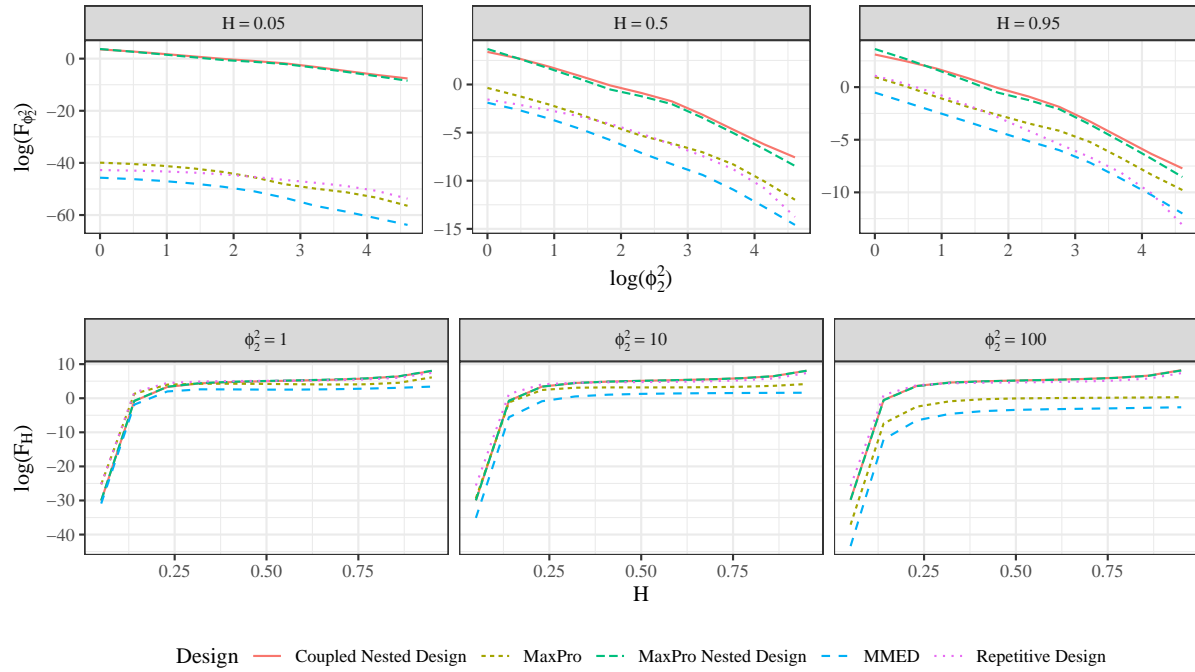


Figure S11: *log of the Fisher information for parameters ϕ_2^2 and H under different ϕ_2^2 and H values.*

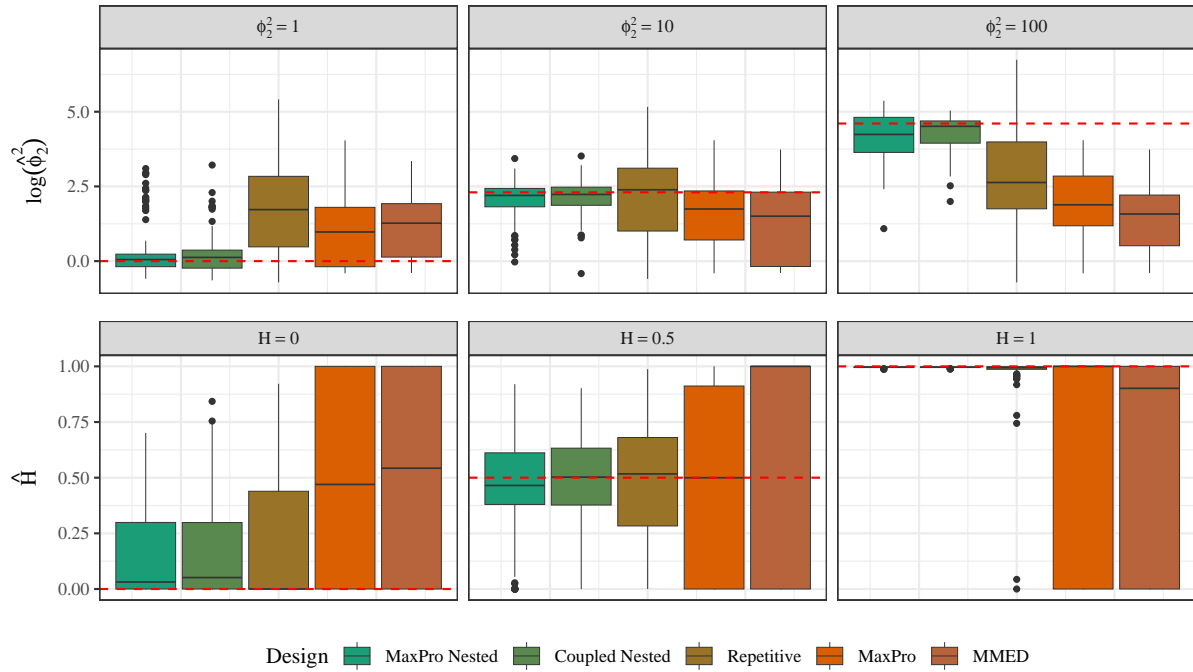


Figure S12: Spread of final estimation of $\log(\hat{\phi}_2^2)$ (top) and H (bottom) across 50 repetitions for different true values ϕ_2^2 and H , with respect to the initial design. The true value for each case is indicated by the red horizontal dashed line.

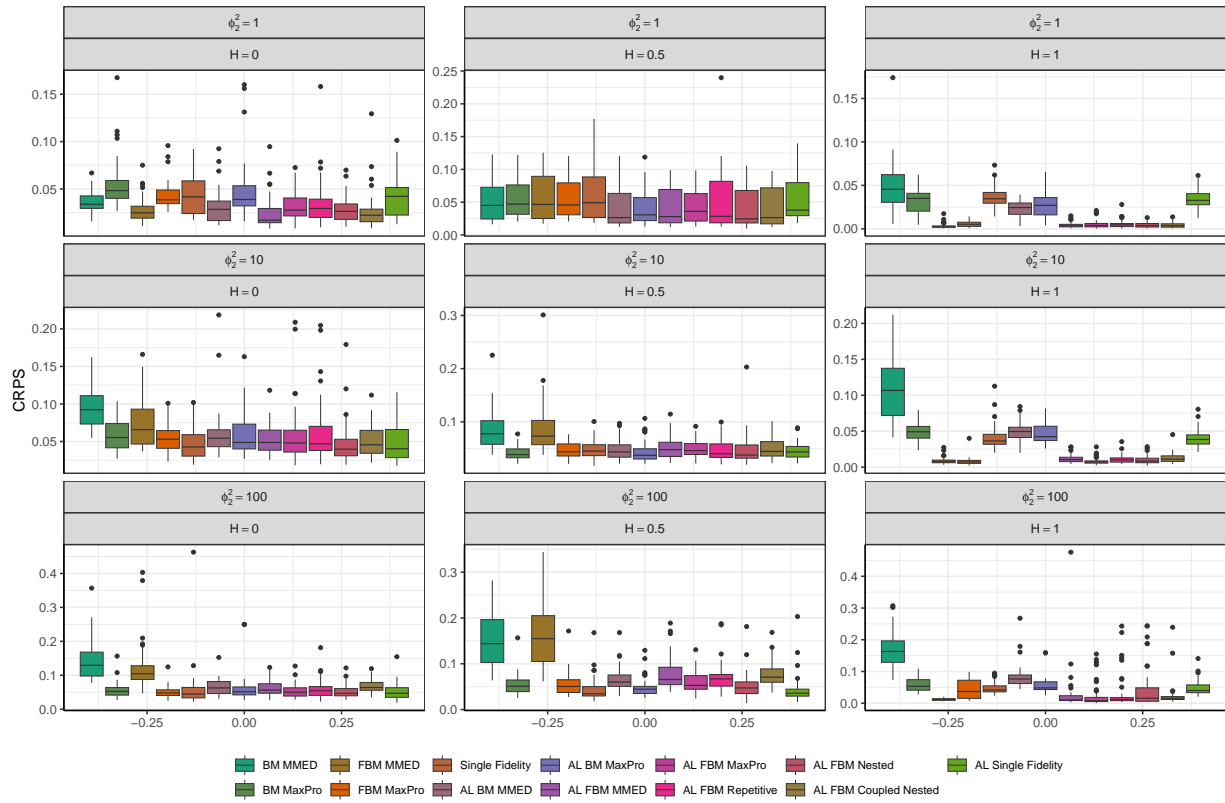


Figure S13: Spread of the final log of the CRPS from the numerical study for each combination of true hyper-parameters and across 50 repetitions for each combination.

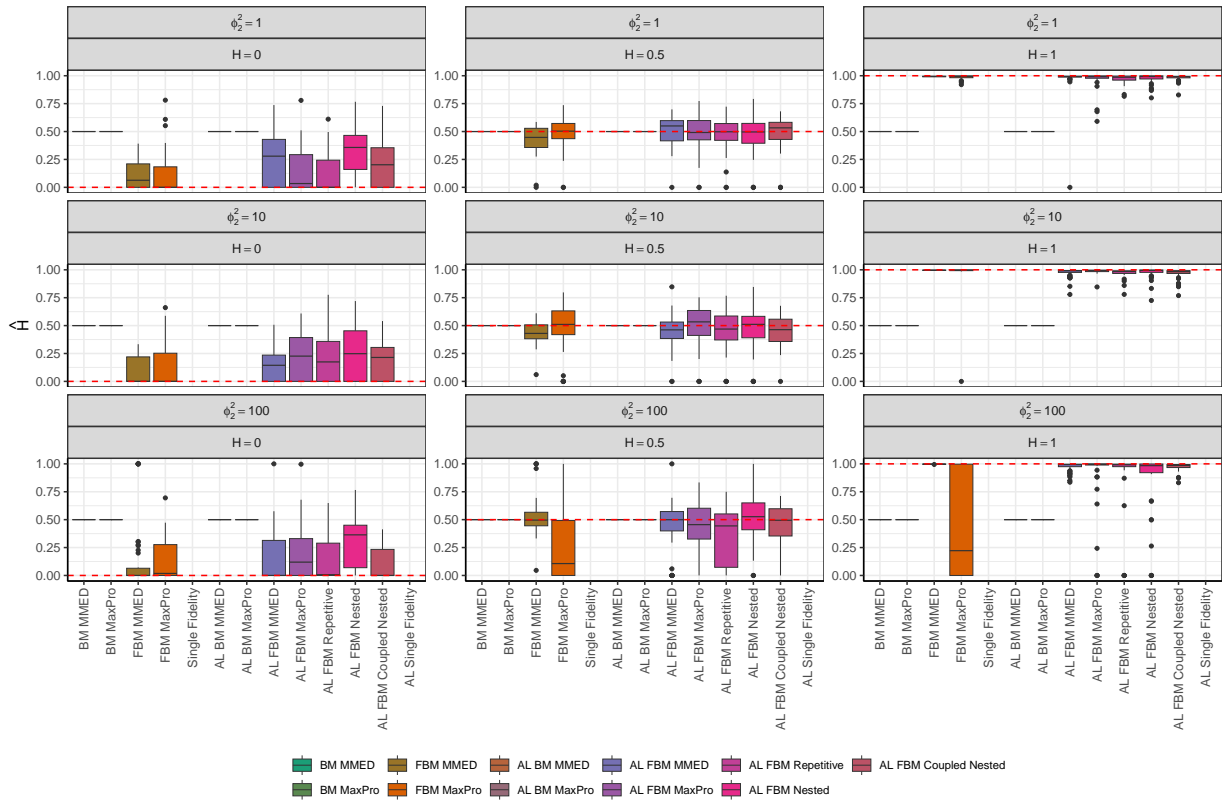


Figure S14: Spread of the final estimation of H from the numerical study for each combination of true hyper-parameters and across 50 repetitions for each combination.

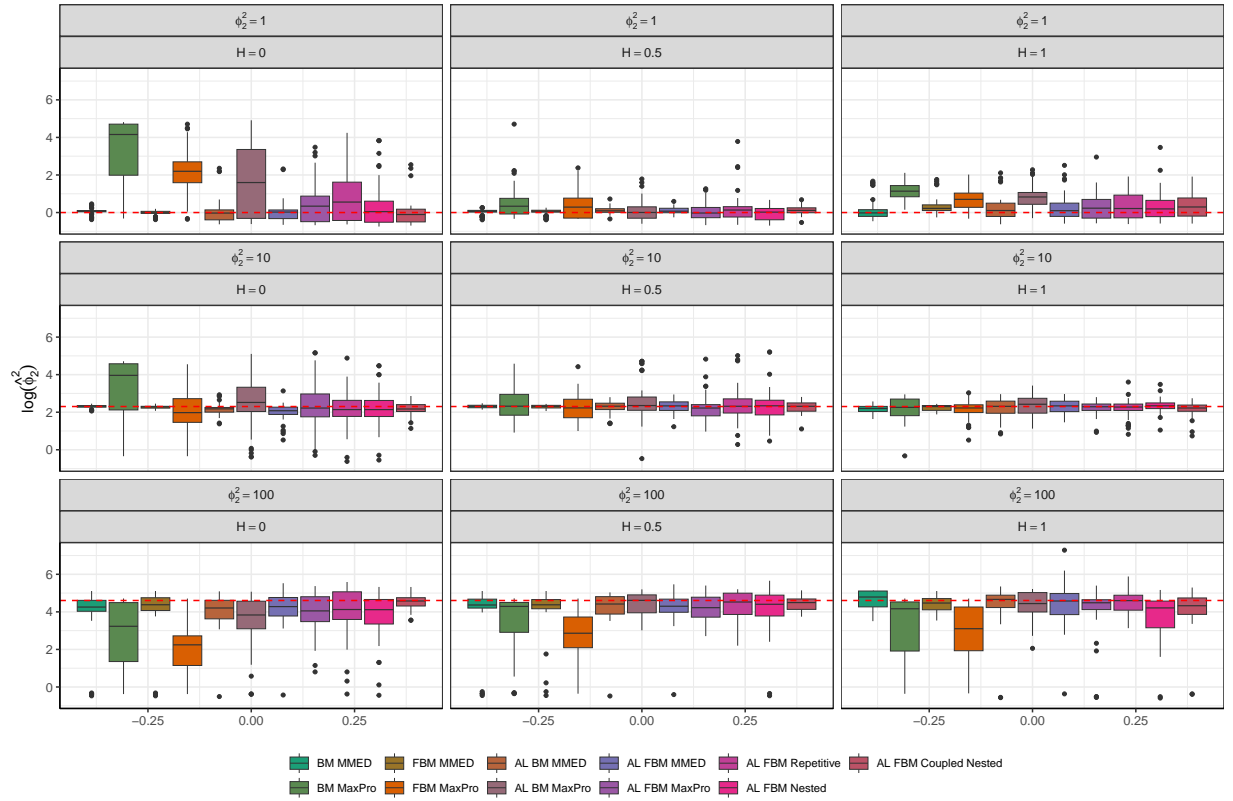


Figure S15: Spread of the final estimation of the log of ϕ_2^2 from the numerical study for each combination of true hyper-parameters and across 50 repetitions for each combination.

F Supporting figures for Section 5

This section provides the supporting figures for Section 5, including the results of the final estimation of H in the Poisson's equation case study (Figure S6), and the jet engine turbine blade case study (Figure S8), as well as the log-log plots from the preliminary study on the jet engine turbine blade FEA simulations (Figure S7).

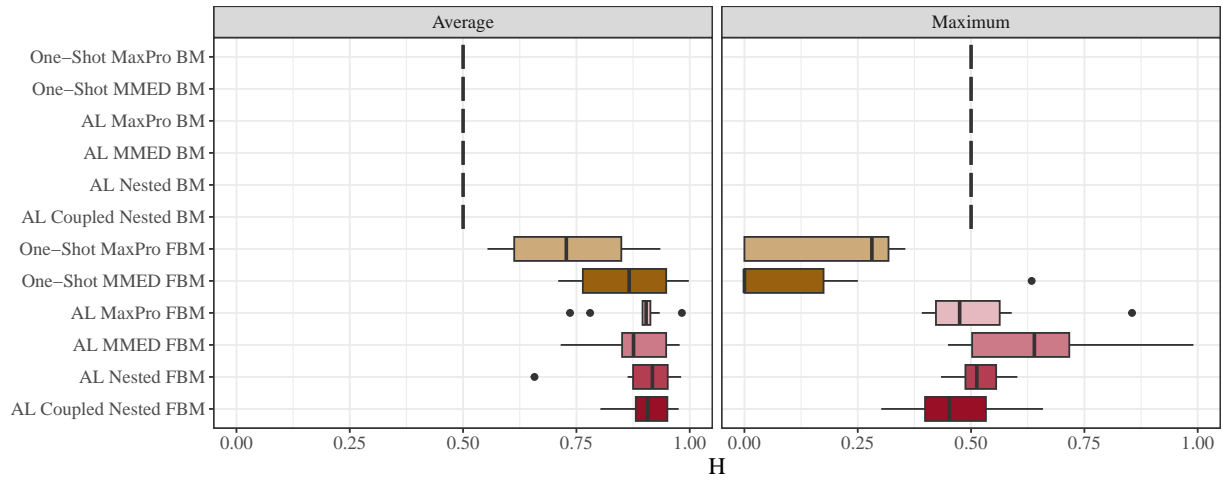


Figure S16: Spread of the final estimation of H from the Poisson's equation case study across 10 repetitions.

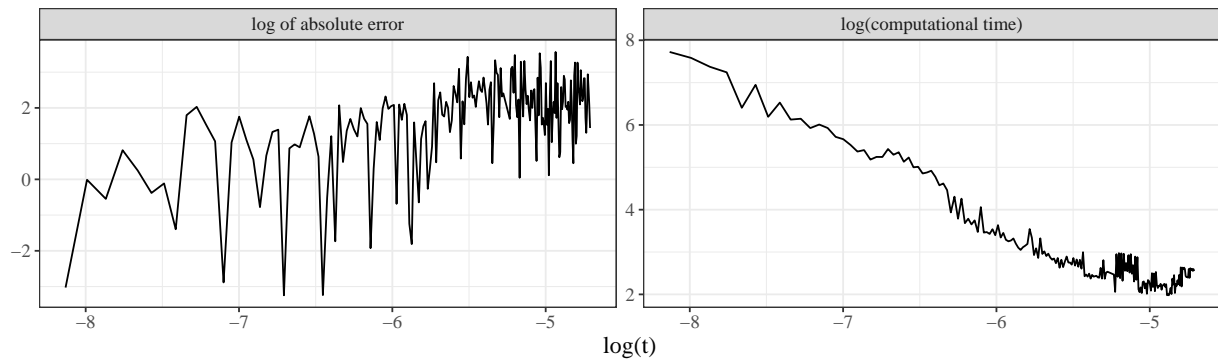


Figure S17: log-log plot of the absolute error of the response of interest (right) and computational time (left) with respect to the mesh size from the jet engine turbine blade case study.

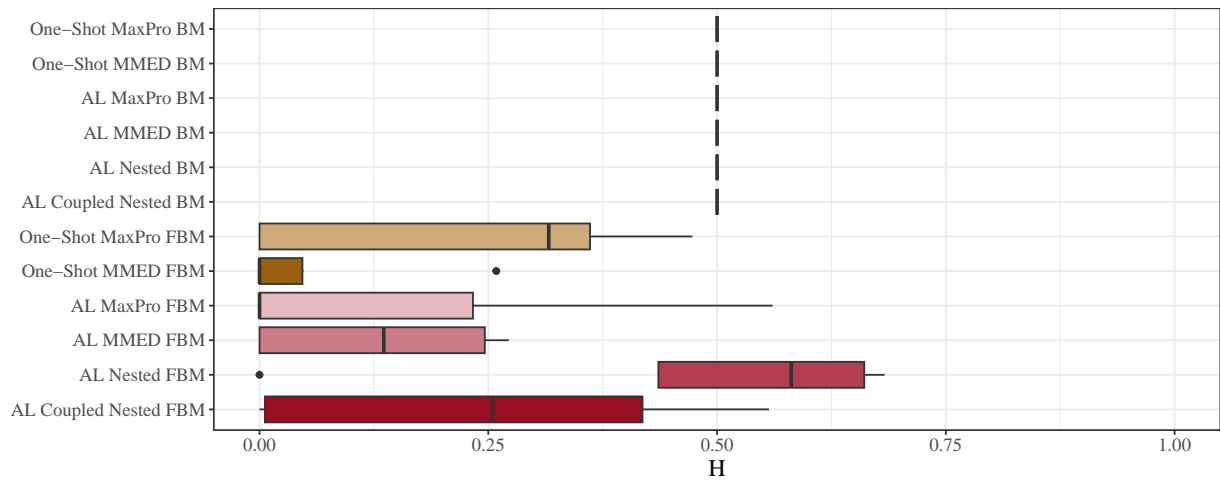


Figure S18: Spread of the final estimation of H from the jet engine turbine blade case study across 5 repetitions.